PUBLICATIONS OF
THE UNIVERSITY OF EASTERN FINLAND

Dissertations in Forestry and Natural Sciences

GERARDO GONZÁLEZ

EDGE-PROMOTING PRIORS IN ELECTRICAL IMPEDANCE TOMOGRAPHY

UNIVERSITY OF
EASTERN FINLAND

PUBLICATIONS OF THE UNIVERSITY OF EASTERN FINLAND
DISSERTATIONS IN FORESTRY AND NATURAL SCIENCES

No 292

Gerardo González

EDGE-PROMOTING PRIORS IN ELECTRICAL IMPEDANCE TOMOGRAPHY

ACADEMIC DISSERTATION

To be presented by the permission of the Faculty of Science and Forestry for public examination in the Auditorium Sn 200 at the University of Eastern Finland, Kuopio, on December 8th, 2017, at 12 o'clock.

University of Eastern Finland
Department of Applied Physics
Kuopio 2017

Grano Oy
Jyväskylä, 2017
Editors: Pertti Pasanen, Pekka Toivanen,
Jukka Tuomela, and Matti Vornanen

Distribution:
University of Eastern Finland Library / Sales of publications
julkaisumyynti@uef.fi
http://www.uef.fi/kirjasto

ISBN: 978-952-61-2671-5 (Print)
ISSNL: 1798-5668
ISSN: 1798-5668
ISBN: 978-952-61-2672-2 (pdf)
ISSNL: 1798-5668
ISSN: 1798-5676

Author's address:
University of Eastern Finland
Department of Applied Physics
P.O.Box 1627
70211 KUOPIO
Finland
email: gerardo.delmuro@uef.fi

Supervisors:
Professor Marko Vauhkonen
University of Eastern Finland
Department of Applied Physics
P.O.Box 1627
70211 KUOPIO
Finland
email: marko.vauhkonen@uef.fi

Senior Researcher Janne Huttunen, Ph.D.
Nokia Technologies
Nokia Labs
Karaportti 4
02610 Espoo
Finland
email: janne.m.huttunen@nokia.com

Professor Ville Kolehmainen
University of Eastern Finland
Department of Applied Physics
P.O.Box 1627
70211 KUOPIO
Finland
email: ville.kolehmainen@uef.fi

Reviewers:

Lecturer Dr. Oliver Dorn
School of Mathematics,
University of Manchester
Oxford Rd
Manchester, M13 9PL
England, United Kingdom
email: oliver.dorn@manchester.ac.uk

Senior Lecturer Dr. Nick Polydorides
School of Engineering,
University of Edinburgh
The King's buildings
Edinburgh, EH93JL
Scotland, United Kingdom
email: n.polydorides@ed.ac.uk

Opponent:

Prof. Dipl.-Ing. Dr. techn. Daniel Watzenig
Technische Universität Graz.
Institut für Regelungs
und Automatisierungstechnik
Inffeldgasse 21/B/I
8010 Graz, Austria
email: daniel.watzenig@tugraz.at

Gerardo González
Edge-Promoting Priors in Electrical Impedance Tomography
Kuopio: University of Eastern Finland, 2017
Publications of the University of Eastern Finland
Dissertations in Forestry and Natural Sciences

ABSTRACT

In electrical impedance tomography (EIT), the admittivity distribution (complex conductivity) is reconstructed based on the boundary measurements of current and voltage. This reconstruction problem is ill-posed and nonlinear. This means that the solutions are highly intolerant towards both measurement noise and modeling errors. Therefore, in order to attain meaningful solutions, tailored reconstruction methods have to be implemented.

In the Bayesian framework, the EIT inverse problem is formulated as a statistical inference problem. This problem is based on the statistical considerations of the *a priori* information about the admittivity and the noise statistics of the measurements. In the statistical approach, the prior information can be, for example, sharp internal boundaries in the admittivity distribution, caused by the interfaces between different materials. In this work, we introduce prior models for removing high oscillations in the admittivity distribution, whilst preserving such internal boundaries. These priors are investigated in three studies.

The first study proposes a fully 3D EIT reconstruction approach for reassembling piecewise regular conductivities using the TV functional. In addition, a simple approach for a systematic selection of the prior parameter in the TV functional, based on a Bayesian interpretation of the TV model, is presented. In this investigation, the reconstructions are computed employing simulated and real EIT measurements. The results demonstrate the robustness of the proposed parameter selection strategy and verify that the use of the TV prior yields sharp reconstructions in 3D EIT.

The second study investigated the use of isotropic and anisotropic total variation (TV) regularization in EIT. In this work, the experiments were designed to demonstrate the role of the choice, between the two versions of the TV functional, has upon the properties of EIT reconstructions. The reconstruction schemes utilize laboratory EIT measurements. The results verify that the use of the isotropic form of TV leads to feasible EIT reconstructions, whereas use of the anisotropic form leads to distortions by aligning the boundaries of the inclusions to the co–ordinate axes.

In the last and third study, two joint prior models (TV augmented with the cross-gradient functional and joint TV) were investigated in the context of the image reconstruction problem in EIT. The prior models in this study considered the mutual spatial similarities of the conductivity and permittivity, whilst promoting, in both estimates. The reconstructions in this study are computed employing sim-

ulated EIT measurements. The results indicate that the quality of the estimates improve significantly in the areas where common spatial similarities are shared.

Overall, the cumulative findings presented in this thesis suggest that edge-preserving and noise-robust reconstructions are achievable by using the reconstruction methods employed. Moreover, the prior models studied in this thesis provide tools to relate spatial characteristics between two parameters (conductivity and permittivity). Hence, the extrapolation of these methods to other tomographic modalities, where two or more parameters are sought, is possible.

Universal Decimal Classification: *519.226, 537.311.6, 621.3.011.2, 621.317.33*
INSPEC Theraurus: *tomography; electric impedance imaging; image reconstruction; inverse problems; nonlinear systems; electrical conductivity; permittivity; Bayes methods*
Yleinen suomalainen asiasanasto: *inversio-ongelmat; bayesilainen menetelmä; tomografia; impedanssitomografia; sähkönjohtavuus*

ACKNOWLEDGEMENTS

The research work of this thesis was carried out in the Department of Applied Physics at the University of Eastern Finland.

Firstly, I would like to thank all of those who contributed the research included in this thesis. In particular, I would like to thank the following people.

I am grateful to my supervisor Professor Marko Vauhkonen for his guidance, patience and constructive feedback during the research. I would also like to express my warmest gratitude to my supervisor Janne Huttunen, PhD, for all the guidance and ideas, and especially for his constant support during the work. I also wish to thank Professor Ville Kolehmainen for his time and valuable ideas.

I acknowledge and thank the official pre-examiners Nick Polydorides, PhD, and Oliver Dorn, PhD for assessing this thesis.

I would also like to thank all the current and former member of the Inverse Problems Group. Especially, Assistant Professor Dr. Christina Brandt, Associate Professor Dong Liu, Antti Lipponen, PhD, Meghdoot Mozumber, PhD, Ville Rimpiläinen, PhD, Danny Smyl, PhD, Matti Hanhela, MSc., and Antti Voss, MSc. for their friendship and for making my stay in Kuopio as a foreigner easier.

Finally, I express my deepest gratitude to my family and friends for their support and help during all of this time. Without your encouragement it would not have been possible accomplished this work.

This study, and the publications presented within it, was supported by the Academy of Finland (Finnish Programme for Center of Excellence in Research 2006-2011 and 2012-2017) and the Doctoral Program in Inverse Problems (formerly the Inverse Problems Graduate School).

Kuopio, September, 2017

Gerardo González

LIST OF PUBLICATIONS

This thesis consists of an overview of the following three original articles which are referred in the text by their Roman numerals **I-III**.

I G. González, J. M. J. Huttunen, V. Kolehmainen, A. Seppänen and M. Vauhkonen, "Experimental evaluation of 3D electrical impedance tomography with total variation prior," *Inverse Problems in Science and Engineering*, *24* **8**,1411–1431 (2016).

II G. González, V. Kolehmainen, A. Seppänen, "Isotropic and anisotropic total variation regularization in electrical impedance tomography," *Computers and Mathematics with Applications*, *74* **3** 564-576 (2017).

III G. González, J. M. J. Huttunen, V. Kolehmainen and M. Vauhkonen, "Joint EIT reconstruction of conductivity and permittivity using structural similarity priors," In review *Inverse Problems in Science and Engineering*, (2017).

AUTHOR'S CONTRIBUTION

The publications selected for this dissertation are original research articles on prior density models applied to image reconstruction problems in electrical impedance tomography. The author of this thesis was principal writer in Publication **I** and Publication **III**. The algorithms and implementations in **I** and **III** were developed by the author of this thesis. In Publication **II**, the author of this thesis contributed to the computation of the numerical results. The results were computed using Matlab® platform in all publications. All the publications in this thesis were the result of a joint work with the co-authors.

TABLE OF CONTENTS

1 Introduction

Electrical impedance tomography (EIT) is an imaging modality in which the admittivity (complex conductivity) of an object is estimated as a spatially distributed parameter. In EIT, electric currents are injected into the targeted body using a set of electrodes attached to its boundary and the resulting electrode voltages are recorded. Based on these measurements, an estimate for the admittivity distribution is computed. This reconstructed admittivity distribution can be then used to derive an image of the target. Extensive literature has been published previously on the applications of EIT in a variety of scientific fields such as process monitoring [1], biomedical imaging [2–5], geology [6], and non-destructive testing [7]. In most of the cases, however, only the real part of the admittivity (conductivity) is estimated, commonly using the amplitude data of the measurements. This technique is often referred to as electrical resistance tomography (ERT) [8].

The admittivity estimation using EIT data is a severely ill-posed and nonlinear inverse problem which makes the solution highly sensitive to both measurement noise and modeling errors. Thus, given the ill-posed nature of the problem, regularization (deterministic framework) or prior information (statistical framework) has to be used to obtain feasible estimates.

Within the Bayesian framework, the regularization is based on the statistical considerations of the *a priori* information about the admittivity as well as the noise statistics of the measurements. The objective in the Bayesian approach is to conduct a statistical inference about the sought admittivity, based on all the available knowledge of the measurements and the prior information known about the admittivity distribution. Hence, the solution to the inverse problem in EIT image reconstruction is the posterior probability distribution, which is the conditional distribution of the unknown admittivity, given the EIT measurement data. For further examples employing the statistical approach, see [9, 10].

In Bayesian based analysis, the formulation of prior probability distributions plays an important role in the estimation process. A prior probability distribution is a distribution that would express *a priori* information about the sought parameter, before any measurement is taken. The main difficulty in constructing prior distributions depends upon which type of *a priori* information is considered. Examples for *a priori* information could be a certain range of values in which the sought parameter only has a physical interpretation or representation, that in a certain basis, is sparse. Sparsity can be understood as a representation of a variable that has a small number of non-zero elements in a suitable basis. Hence, it is a useful feature which can impact directly the efficiency of the computational methods employed, by reducing its complexity.

Several studies have shown that regularization methods employing ℓ_1-norm

promote sparsity [11–13]. Particularly in the image reconstruction problem in EIT, it has been shown in [14,15] that representing the in homogeneities in a conductivity distribution with a sparse basis provides sharper reconstructions. Similarly, regularization methods employing the total variation (TV) functional allows for the reconstruction of sharp interfaces in the solutions. TV regularization was originally deployed to solve the image denoising problem [11]. Since then, it has been applied to reconstruct piecewise regular images in many tomography modalities, such as electrical capacitance tomography [16–19], positron emission tomography [20], diffuse optical tomography [21,22] and computerized tomography [23–25].

In EIT, TV regularization has been utilized in several previous studies. For example, the reconstruction method for 2D EIT, using a differentiable approximation of TV funcitonal, was studied in [13]. In [26], the Markov chain Monte Carlo method was used to estimate the mean of the posterior probability density for 2D EIT, using a TV prior model for the conductivity. Some methods allow the use of the exact (non-differentiable) TV functional. For example, in [27], an optimization algorithm for TV regularized EIT based on the primal dual interior point framework was introduced. A similar approach was applied for difference imaging in [28]. Finally, 3D EIT reconstruction methods have been proposed in [29] and [30].

Generalizations of the TV functional have been proposed to handle vector-valued images [31–33]. Vector-valued images, can be thought as a group of scalar images which may carry structural similarities between each other. The results in these studies have indicated that exploiting structural similarity between image components, in a joint reconstruction scheme, can yield better and sharper structures in the reconstructed images, than using regularization functionals for each image component independently.

In the context of the EIT image reconstruction problem, current approaches have focused on estimating conductivity and permittivity independently. However, in many practical situations one can expect solutions with spatial similarities in the sense that the solutions have the same alignment of boundaries and are at the same location. For example, if the conductivity has a jump at a material interface, it is reasonable to expect a jump at the same location in the permittivity. Hence, the prior densities which relate spatial similarities between the conductivity and permittivity would be advantageous in a reconstruction scheme for recovering sharper structures utilizing both parameters.

The main goal of this thesis is to study prior models which promote well-defined edges in the conductivity and permittivity distributions using EIT data. This work consists of three publications in which the studies are presented with details. The aim and content of each study were:

1. To demonstrate the applicability of the TV regularization approach in a 3D EIT set up. In addition, a parameter selection strategy for the TV prior, based on the *a priori* information of materials in the target and their conductivity ranges, was introduced. The proposed approach for selecting the

scaling parameter in the prior model, in a reconstruction scheme employing the TV functional, is evaluated both with simulated and experimental measurements. (**I**)

2. To study the effect of two widely used forms of TV regularization (isotropic and anisotropic TV) in EIT. This effect is investigated based on a set of simulations as well as laboratory experiments in a 2D setting. (**II**)

3. To investigate the feasibility of using a joint reconstruction of the conductivity and permittivity distribution in EIT image reconstruction problem employing two prior models based on generalization of the TV functional. Here, the two prior models are based on the *a priori* knowledge that the conductivity and permittivity are likely to show similar structures. The approach is tested with simulated EIT measurements in a 2D setting. (**III**)

The content of this thesis is as follows. A brief review of the EIT forward model is given in Chapter 2. In this chapter, the image reconstruction problem of EIT is also concisely explained. Chapter 3 describes briefly a family of prior models based on Gibbs probability distributions for Bayesian inversion, which relies on l_p norms. In this chapter, two prior models, based on the TV functional, namely: TV with cross gradient constraints (TVCG) and joint total variation (JTV) are introduced. In Chapter 4, the review of the results of the three publications is given. A summary and conclusions of this thesis are given in Chapter 5.

2 Electrical Impedance Tomography

In this chapter, a short introduction to the admittivity estimation problem in EIT is given. In Section 2.1, the forward model and a numerical implementation of the model are explained. Section 2.2 contains a brief review of the inversion methods utilized in EIT. The absolute imaging is discussed in Section 2.2.2 and difference imaging in Section 2.2.3. For more extensive reviews of EIT reconstruction methods, see [34–38].

2.1 FORWARD MODEL AND NOTATION

EIT is a diffusive imaging modality in which the forward problem consists of computing the electrode voltages when the admittivity, currents and contact impedances are given. A schematic representation of an EIT experiment is shown in Figure 2.1. In the estimation of the admittivity in EIT, a mathematical model that predicts the measurements, given the admittivity, is needed. The *complete electrode model* (CEM) [39] is the best available measurement model for EIT measurements. The CEM is of the form

$$\begin{aligned}
\nabla \cdot \Big(\gamma(\omega)\nabla u\Big) &= 0, && x \text{ in } \Omega, && (2.1)\\
u + z^{(\ell)}\,\gamma(\omega)\frac{\partial u}{\partial \vec{n}} &= \mathrm{U}^{(\ell)}, && x \in e^{(\ell)},\ \ell = 1,2,\ldots,L && (2.2)\\
\gamma(\omega)\frac{\partial u}{\partial \vec{n}} &= 0, && x \in \partial\Omega \setminus \cup_{\ell=1}^{L} e^{(\ell)} && (2.3)\\
\int_{e^{(\ell)}} \gamma(\omega)\frac{\partial u}{\partial \vec{n}}\mathrm{d}S &= I^{(\ell)}, && \ell = 1,2,\ldots,L && (2.4)
\end{aligned}$$

where the angular frequency is $\omega = 2\pi f$ and f is the frequency of the injected current. The target domain is denoted by $\Omega \subset \mathbb{R}^n$, where $n = 2, 3$. The boundary of Ω is $\partial\Omega$. The admittivity distribution is given as $\gamma = \sigma(x;\omega) + i\omega\varepsilon(x;\omega)$, where $\sigma(x;\omega)$ is the conductivity and $\varepsilon(x;\omega)$ is the permittivity. The potential in Ω is denoted by $u = u(x)$, and L is the number of electrodes $e^{(\ell)}$. Moreover, $I^{(\ell)}$ and $\mathrm{U}^{(\ell)}$ are the electric current and potential on $e^{(\ell)}$, respectively. $z^{(\ell)}$ is the contact impedance corresponding to the ℓ^{th} electrode $e^{(\ell)}$. Furthermore, we set

$$\sum_{\ell=1}^{L} I^{(\ell)} = 0 \quad \text{and} \quad \sum_{\ell=1}^{L} \mathrm{U}^{(\ell)} = 0, \tag{2.5}$$

where the first condition is the conservation of charges and the second condition is a choice for the ground potential level that ensures the uniqueness of

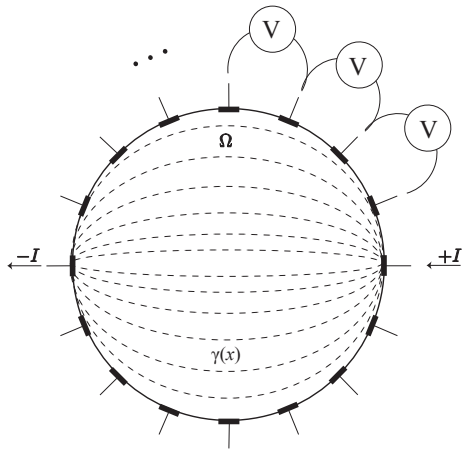

Figure 2.1: EIT measurement diagram corresponding to one current injections.

the solution [40, 41]. Lastly, the electrode potential vector is defined as $\mathrm{U} = (\mathrm{U}^{(1)}, ..., \mathrm{U}^{(L)})^\top$ with $\mathrm{U} \in \mathbb{C}^L$.

2.1.1 Finite element approximation of the forward problem

In this study, the solution of the CEM is approximated by employing the finite element method (FEM). The approach described in [41] is modified accordingly to add the permittivity term (imaginary part of the admittivity) into the modeling. In the finite element (FE) implementation of the CEM, the admittivity $\gamma(x;\omega)$ is approximated by

$$\sigma(x;\omega) \approx \sum_{i=1}^{N_1} \sigma_{d,i}(\omega)\phi_i(x), \quad \text{and} \quad \varepsilon(x;\omega) \approx \sum_{i=1}^{N_1} \varepsilon_{d,i}(\omega)\phi_i(x). \tag{2.6}$$

The functions ϕ_i are piecewise linear basis functions for the conductivity and the permittivity. N_1 is the number of first-order nodes in FEM representation. The corresponding finite dimensional representation of the conductivity and permittivity are denoted respectively by $\sigma_d(\omega) = \big(\sigma_{d,1}(\omega), \ldots, \sigma_{d,N_1}(\omega)\big)^\top \in \mathbb{R}^{N_1}$ and $\varepsilon_d(\omega) = \big(\varepsilon_{d,1}(\omega), \ldots, \varepsilon_{d,N_1}(\omega)\big)^\top \in \mathbb{R}^{N_1}$. The potential u is approximated as

$$u(x;\omega) \approx \sum_{i=1}^{N_2} c_i(\omega)\psi_i(x), \qquad c_i(\omega) \in \mathbb{C} \tag{2.7}$$

where ψ_i are basis functions for the electric potential and are chosen to be second-order (piecewise) polynomials. N_2 is the number of second-order nodes in FEM representation.

2.1.2 Conventional noise model

Typically, the measurement noise is modeled in EIT as Gaussian and additive which is mutually independent with the unknown admittivity. Using this noise model, the *additive observation model* for voltage data, at the given angular frequency ω, can be written as

$$U = H\Big(\sigma_d(\omega), \varepsilon_d(\omega)\Big) + e, \qquad e \sim \mathcal{N}(e_*, \Gamma_e), \tag{2.8}$$

where the data vector

$$U = (\mathrm{re(U)}, \mathrm{im(U)})^\top$$

consists of the real and imaginary parts of the measured electrode potentials, $H\big(\sigma_d(\omega), \varepsilon_d(\omega)\big)$ is a mapping resulting from the FE approximation of the CEM, and e is Gaussian distributed noise with covariance matrix Γ_e and mean e_*.

2.2 INVERSE PROBLEM IN EIT

As it has been discussed in previous sections, the forward problem in EIT is to compute the electrode potentials when the admittivity, injected currents, and the contact impedances are known. Conversely, the inverse problem is to reconstruct the admittivity distribution based on noisy electrode potential differences.

In this thesis, the admittivity is assumed to be time invariant during the acquisition of the set of measurements. For the non-stationary reconstruction problem in EIT, see for example [42–44].

2.2.1 EIT as a statistical estimation problem

In Bayesian formalism, the reconstruction problem of EIT is treated as a statistical inference problem. Here, both voltage measurements and the discretized admittivity distribution are modeled as random variables. The information about the unknown variables is then modeled as a joint probability density called the prior density. This density contains all the information available about the unknown variables prior to the measurements.

The solution to the statistical inverse problem is the posterior distribution. The posterior density is given by the Bayes' formula and can be written as

$$\pi(\sigma_d, \varepsilon_d | U) = \frac{\pi(U|\sigma_d, \varepsilon_d)\pi(\sigma_d, \varepsilon_d)}{\pi(U)} \tag{2.9}$$

where $\pi(U|\sigma_d, \varepsilon_d)$ is the likelihood density, $\pi(\sigma_d, \varepsilon_d)$ the prior density and $\pi(U)$ is normalization constant. The normalization constant can often be neglected and Equation (2.9) simplifies to the form

$$\pi(\sigma_d, \varepsilon_d | U) \propto \pi(U|\sigma_d, \varepsilon_d)\pi(\sigma_d, \varepsilon_d). \tag{2.10}$$

The likelihood density $\pi(U|\sigma_d, \varepsilon_d)$ is a conditional probability density of the measurements given the parameters σ_d and ε_d. In this work, the parameters σ_d and ε_d and the noise e are assumed to be independent. Using the observation model (2.8), the likelihood density is obtained as

$$\pi(U|\sigma_d, \varepsilon_d) = \pi_e\Big(U - H\Big(\sigma_d(\omega), \varepsilon_d(\omega)\Big)\Big) \tag{2.11}$$

where π_e is the probability density of the additive noise e. Hence, the likelihood density can be written as

$$\begin{aligned}\pi(U|\sigma_d, \varepsilon_d) \quad = \quad & \frac{(\det \Gamma_e)^{-1/2}}{2\pi^{n/2}} \exp\Big(-\frac{1}{2}\Big(U - H\Big(\sigma_d(\omega), \varepsilon_d(\omega)\Big) - e_*\Big)^\top \cdot \\ & {\Gamma_e}^{-1}\Big(U - H\Big(\sigma_d(\omega), \varepsilon_d(\omega)\Big) - e_*\Big),\end{aligned} \tag{2.12}$$

where $\det \Gamma_e$ denotes the determinant of the measurement noise covariance matrix Γ_e. In this work, the expectation of the noise is $e_* = 0$.

The prior distribution $\pi(\sigma_d, \varepsilon_d)$ represents the knowledge of the unknowns based on prior information. Here, we consider a family of densities which can be written in the form

$$\pi(\sigma_d, \varepsilon_d) = \pi_+(\sigma_d, \varepsilon_d) \exp\Big(-F(\sigma_d, \varepsilon_d)\Big) \tag{2.13}$$

where the functional F is defined in the following chapter. The prior contains the positivity constraint $\pi_+(\sigma_d, \varepsilon_d)$. This constraint is to restrict the values of the conductivities and permittivities to a certain range of values. For instance, the conductivities and permittivities cannot be negative. Given the likelihood and prior models as above, the posterior can be written as

$$\begin{aligned}\pi(\sigma_d, \varepsilon_d|U) \quad \propto \quad & \pi_+(\sigma_d, \varepsilon_d) \exp\Bigg(-\frac{1}{2}\Big(U - H\Big(\sigma_d(\omega), \varepsilon_d(\omega)\Big)\Big)^\top \\ & {\Gamma_e}^{-1}\Big(U - H\Big(\sigma_d(\omega), \varepsilon_d(\omega)\Big)\Big) - F(\sigma_d, \varepsilon_d)\Bigg).\end{aligned} \tag{2.14}$$

To make an inference and visualize the solution, point estimates can be computed from the posterior density $\pi(\sigma_d, \varepsilon_d|U)$. The most common point estimates are the *conditional mean* (CM) and the *maximum a posteriori* (MAP). The CM estimate is the expectation of the posterior distribution and it typically requires the use of computation time intensive Markov chain Monte Carlo (MCMC) methods (see e.g. [26]). In this thesis, the MAP estimate

$$(\sigma_d, \varepsilon_d)_{\text{MAP}} \quad = \quad \arg\max_{\sigma_d,\, \varepsilon_d}\Big\{\pi(\sigma_d, \varepsilon_d|U)\Big\} \tag{2.15}$$

is employed. Given the previous assumptions, the computation of the MAP estimate coincides with the solution of the following constrained minimization problem

$$(\sigma_d, \varepsilon_d)_{\text{MAP}} = \underset{\substack{\sigma_{d,i}>0 \\ \varepsilon_{d,i}>0}}{\arg\min} \Big\{ \mathcal{F}(\sigma_d, \varepsilon_d; U) \Big\}. \tag{2.16}$$

where the functional $\mathcal{F}$ is written as

$$\begin{aligned} \mathcal{F}(\sigma_d, \varepsilon_d; U) &= \left(-\frac{1}{2}\Big(U - H\Big(\sigma_d(\omega), \varepsilon_d(\omega)\Big)\Big) \right)^{\top} {\Gamma_e}^{-1} \\ &\quad \left(U - H\Big(\sigma_d(\omega), \varepsilon_d(\omega)\Big)\right) + F(\sigma_d, \varepsilon_d) \Big) \\ &= \left\| L_e \Big(U - H\Big(\sigma_d(\omega), \varepsilon_d(\omega)\Big)\Big) \right\|^2 + F(\sigma_d, \varepsilon_d), \end{aligned} \tag{2.17}$$

where L_e is the Cholesky factor of the inverse covariance matrix, i.e. ${\Gamma_e}^{-1} = L_e^{\top} L_e$.

Barrier Methods for Constrained Optimization

In order to handle the positivity constraint of the conductivity and permittivity, we reformulate the problem (2.16) as a sequence of unconstrained problems utilizing a barrier function [45]. In barrier methods, the constraints are incorporated into the objective function in a process called *dualizing* the constraints. In this case, the objective function is augmented with a *barrier function*. The barrier function will favor points in the interior of the feasible region S over those near the boundary of S. In other words, as a feasible point approaches one of the boundaries inside the feasible region, the barrier function approaches to infinity.

Let be $b : S \subset \mathbb{R}^n \to \mathbb{R}$ a barrier function with the following properties:

(a) $b \in \mathbf{C}(S)$ where $S = \{x \in \mathbb{R}^n \mid g_i(x) \leq 0,\ i = 1, \ldots, n\}$ and $g_i(x)$ is a twice-continuously differentiable function in $\mathbb{R}^n$.

(b) if $\{x_i\}$ is any finite sequence of points in S converging to x such that $g_i(x) = 0$ for at least one i then $\lim_{k\to\infty} b(x_k) = \infty$.

Two common examples of barrier functions are

$$b(x) = -\sum_{i=1}^{N_1} \log\Big(g_i(x)\Big) \qquad \text{and} \tag{2.18}$$

$$b(x) = -\sum_{i=1}^{N_1} \frac{1}{g_i(x)}. \tag{2.19}$$

By selecting the equation (2.18), the unconstrained problem is written as

$$(\sigma_d, \varepsilon_d)^{(k)}_{\text{MAP}} = \underset{\sigma_d,\, \varepsilon_d}{\arg\min} \left\{ \mathcal{F}^{(k)}(\sigma_d, \varepsilon_d; U) \right\}, \tag{2.20}$$

where the functional $\mathcal{F}^{(k)}$ is replaced by

$$\begin{aligned} \mathcal{F}^{(k)}(\sigma_d, \varepsilon_d; U) &= \left\| L_e \left(U - H\left(\sigma_d(\omega), \varepsilon_d(\omega)\right) \right) \right\|^2 + F(\sigma_d, \varepsilon_d) \\ &\quad - \mu^{(k)} \sum_{i=1}^{N_1} \left(\log(\sigma_{d,i}) + \log(\varepsilon_{d,i}) \right). \end{aligned} \tag{2.21}$$

When the sequence of the parameters $\left\{ \mu^{(k)} \right\}_{k \in \mathbb{N}}$ is selected such that

$$0 < \mu^{(k+1)} \leq \mu^{(k)} \text{ and } \mu^{(k)} \to 0 \text{ as } k \to \infty, \tag{2.22}$$

the solution $(\sigma_d, \varepsilon_d)^{(k)}_{\text{MAP}}$ converges to the solution of the constrained problem as $k \to \infty$. For a general view on the barrier methods see [**?**, 45]

2.2.2 Absolute imaging

Absolute imaging refers to a method in which the admittivity is reconstructed using a single set of voltage measurements. Most of the approaches state the reconstruction problem in absolute imaging as an optimization problem such as (2.20). Typically, the search for the minimizer is conducted using gradient based methods. The most common algorithm employed for finding the minimizer of (2.20) is the Gauss-Newton (GN) method for *nonlinear least-squares problems* [47, 48].

The GN method can be derived from Newton's original method for function optimization via an approximation. The formula for Newton's method for minimizing a functional $\mathcal{F}$ of parameters $\theta = \begin{bmatrix} \sigma_d \\ \varepsilon_d \end{bmatrix}$ is

$$\theta^{(i+1)} = \theta^{(i)} - \kappa\, \delta^{(i)}_\theta \tag{2.23}$$

where κ is the step size in the search direction which in turn is given by

$$\begin{aligned} \delta^{(i)}_\theta &= \left((J^{(i)})^\top \Gamma_e^{-1} J^{(i)} + \frac{\partial^2 F}{\partial \theta^2}\left(\theta^{(i)}\right) + \frac{\partial^2 b}{\partial \theta^2}\left(\theta^{(i)}\right) \right)^{-1} \\ &\cdot \left((J^{(i)})^\top \Gamma_e^{-1} \left(U - H\left(\theta^{(i)}\right) \right) - \frac{\partial F}{\partial \theta}\left(\theta^{(i)}\right) - \frac{\partial b}{\partial \theta}\left(\theta^{(i)}\right) \right) \end{aligned} \tag{2.24}$$

where $\frac{\partial^2 F}{\partial \theta^2} = \operatorname{diag}\left(\frac{\partial^2 F}{\partial \sigma_d^2}, \frac{\partial^2 F}{\partial \varepsilon_d^2} \right)$ and $\frac{\partial F}{\partial \theta} = \left(\frac{\partial F}{\partial \sigma_d}, \frac{\partial F}{\partial \varepsilon_d} \right)^\top$ are the block diagonal Hessian matrix and the gradient of the functional F, respectively. The term $J^{(i)}$ is

the Jacobian matrix of the forward mapping $\theta^{(i)} \mapsto H\left(\theta^{(i)}\right)$ written in the form of a block matrix, such that $J^{(i)} = (J_{\sigma_d}, J_{\varepsilon_d})$, where the block matrices are

$$J_{\sigma_d} = \left.\frac{\partial H(\sigma_d, \varepsilon_d; w)}{\partial \sigma_d}\right|_{\sigma_d^{(i)}, \varepsilon_d^{(i)}} \qquad J_{\varepsilon_d} = \left.\frac{\partial H(\sigma_d, \varepsilon_d; w)}{\partial \varepsilon_d}\right|_{\sigma_d^{(i)}, \varepsilon_d^{(i)}}.$$

The computation of the Jacobian blocks J_{σ_d} and J_{ε_d} are presented in [49]. The Hessian matrix and the gradient of the barrier function are given by $\frac{\partial^2 b}{\partial \theta^2}$ and $\frac{\partial b}{\partial \theta}$, respectively. Lastly, the GN method can be equipped with a line search, as exemplified in [47]. For more details on the applied GN method and other optimization methods in EIT, refer to, for an example, [49].

2.2.3 Difference imaging

In difference imaging [4, 8, 36, 50–56], the goal is to reconstruct the change in the conductivity and permittivity between EIT measurements at two time instants. Namely,

$$\Delta\sigma_d = \sigma_d^{(2)} - \sigma_d^{(1)}, \tag{2.25}$$

$$\Delta\varepsilon_d = \varepsilon_d^{(2)} - \varepsilon_d^{(1)}. \tag{2.26}$$

Using Equation (2.8), the observation models for two time instants become

$$U(\sigma_d^{(1)}, \varepsilon_d^{(1)}) = H\left(\sigma_d^{(1)}, \varepsilon_d^{(1)}\right) + e_1, \tag{2.27}$$

$$U(\sigma_d^{(2)}, \varepsilon_d^{(2)}) = H\left(\sigma_d^{(2)}, \varepsilon_d^{(2)}\right) + e_2, \tag{2.28}$$

where $e_i \sim \mathcal{N}(e_*, \Gamma_i)$ for $i = \{1, 2\}$.

Usually, the image reconstruction employing difference imaging is achieved by subtracting the two measurements and conducting a global linearization of the nonlinear forward problem. In other words, the observation models (2.27) are approximated by the first order Taylor approximations as

$$U_i \approx H\left(\sigma_d^{(0)}, \varepsilon_d^{(0)}\right) + J_{\sigma_d}\left(\sigma_d^{(i)} - \sigma_d^{(0)}\right) + J_{\varepsilon_d}\left(\varepsilon_d^{(i)} - \varepsilon_d^{(0)}\right) + \ldots \tag{2.29}$$

where the Jacobian blocks $J_{\sigma_d} = \frac{\partial H}{\partial \sigma_d}$ and $J_{\varepsilon_d} = \frac{\partial H}{\partial \varepsilon_d}$ are evaluated on the linearization point $\left(\sigma_d^{(0)}, \varepsilon_d^{(0)}\right)$. By employing these linearizations as well as U_1 and U_2, the resulting observation model is given by

$$\Delta U = J_{\sigma_d}\Delta\sigma_d + J_{\varepsilon_d}\Delta\varepsilon_d + \Delta e \tag{2.30}$$

where $\Delta U = U_2 - U_1$ and $\Delta e = e_2 - e_1$.

Given the observation model (2.30), the corresponding minimization problem is

$$(\widehat{\Delta\sigma_d}, \widehat{\Delta\varepsilon_d}) = \underset{\Delta\sigma_d,\, \Delta\varepsilon_d}{\arg\min} \Big\{ \Big\| L_{\Delta e}(\Delta U - J_{\sigma_d}\Delta\sigma_d - J_{\varepsilon_d}\Delta\varepsilon_d) \Big\|^2 + F(\delta\sigma_d,\, \Delta\varepsilon_d) \Big\}. \tag{2.31}$$

where the matrix $L_{\Delta e}$ is the Cholesky factor of the inverse covariance matrix $\Gamma_{\Delta e}^{-1}$ and the covariance matrix for the difference imaging approach is $\Gamma_{\Delta e} = \Gamma_{e_1} + \Gamma_{e_2}$.

An advantage in the difference image reconstruction scheme is that the computational time is reduced. It also has reasonably good tolerance against modeling errors. In spite of the advantages, this approach is limited in that it is only capable of handling small deviations from the initial conductivity and permittivity [57].

3 Edge-promoting priors in EIT

This chapter consists of a review of three edge-promoting prior models, namely the total variation (TV) prior model, the total variation augmented with cross gradient functional, and the joint total variation. In this thesis, the construction of such priors are considered for the parameter $f = [a_1, \ldots, a_n]^\top$ as the finite dimensional approximation of a function f^∞. For example, f^∞ can be approximated with a piecewise linear representation on a triangular mesh [41]

$$f^\infty(x) \approx \sum_{i=1}^{m} a_i \, \phi_i(x) \tag{3.1}$$

where $\phi_i(x)$ are linear first order basis functions of the triangle elements, or with a piecewise constant discretization on a lattice of regular square pixels $\Omega \subset \bigcup_{i=1}^{m} G_i$ which leads to an approximation

$$f^\infty(x) \approx \sum_{i=1}^{m} a_i \, \chi_{G_i}(x) \tag{3.2}$$

with n pixels within or partially intersecting Ω and where $\chi_{G_i}(x)$ is the characteristic function taking the value of 1 when x in G_i and zero otherwise.

3.1 ℓ_p^q PRIORS

In this work, priors belonging to a certain type of exponential prior, based on ℓ_p norms, are considered. A typical construction of these priors is given by

$$\pi_{prior}(f) \propto \exp\left(-\lambda \|D(f)\|_p^q\right) = \exp\left(-\lambda \left(\sum_{i=1}^{n} |D_i(f)|^p\right)^{q/p}\right) \tag{3.3}$$

where $D_i \in \mathbb{R}^n$ is the i-th column of a linear mapping D. Typically, D can be thought of as the discrete approximation of the differential operator.

The properties of ℓ_p^q priors are determined by the scalar parameters λ, p, and q. To illustrate such properties, level sets and radial profiles of priors corresponding to different choices of λ, p, and q are shown in Figure 3.1. As it can been seen from the figure, the shape of the level-sets is defined by p. The radial profile of $\pi_{prior}(f)$ (i.e. the 1D distribution conditioned along a certain direction) is determined by q. The prior parameter λ controls the scale of $\pi_{prior}(f)$. Furthermore, the properties of these priors will define the posterior density function. An example on how the shape of the posterior is determined employing ℓ_1^1 (or

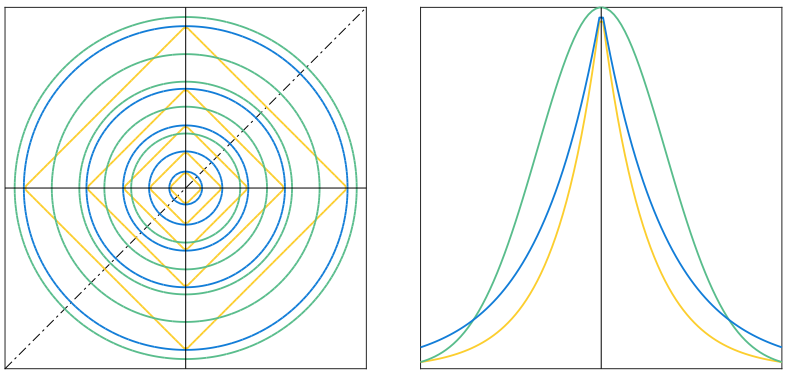

(a) (b)

Figure 3.1: (a) Level sets of different (unnormalized) ℓ_p^q priors for the values $\{1/6, 2/6, \ldots, 1\}$. Yellow lines: $p = q = 1$, $\lambda = 2$. Green lines: $p = q = 2$, $\lambda = 2$. Blue lines: $p = 2$, $q = 1$, $\lambda = 2$. (b) Radial profiles conditioned along the black line $(x = y)$ in (a).

simply ℓ_1) and ℓ_2^2 priors is illustrated in Figure 3.2. In this example, when comparing the MAP estimate, we can observe in Figure(3.2)-(a) that due to the shape of the ℓ_1 prior, the MAP estimate (blue star) lies on the horizontal coordinate axis, which means that the component in vertical direction is zero. In the case of ℓ_2^2 (Gaussian prior), Figure(3.2)-(b), the MAP estimate lies on the first quadrant of the coordinate system.

In Bayesian inference, prior distributions based on the ℓ_1-norm of the parameters are of considerable interest. The reason behind this relies on the properties of such priors since they promote parameter fields with less regularity than Gaussian priors (e.g., discontinuities and blockiness).

Examples of ℓ_1-type priors include the total variation (TV) prior [11], TV based priors [58], and wavelet-based Besov B_{11}^1 priors [59, 60].

3.1.1 Gaussian case

A Gaussian prior can be obtained by the selecting the ℓ_2 norm

$$\begin{aligned} \pi_{prior}(f) &\propto \exp\left(-\lambda \|Lf\|_2^2\right) = \exp\left(-\frac{1}{2} f^\top \left(2\lambda L^\top L\right) f\right) \\ &\propto exp\left(-\frac{1}{2} f^\top \Gamma^{-1} f\right). \end{aligned} \tag{3.4}$$

where $\Gamma = (2\lambda L^\top L)^{-1}$ is the covariance matrix and L is a symmetric and positive definite regularization matrix. Gaussian priors are important in Bayesian modeling. Using Gaussians for both likelihood and prior distribution can facilitate the

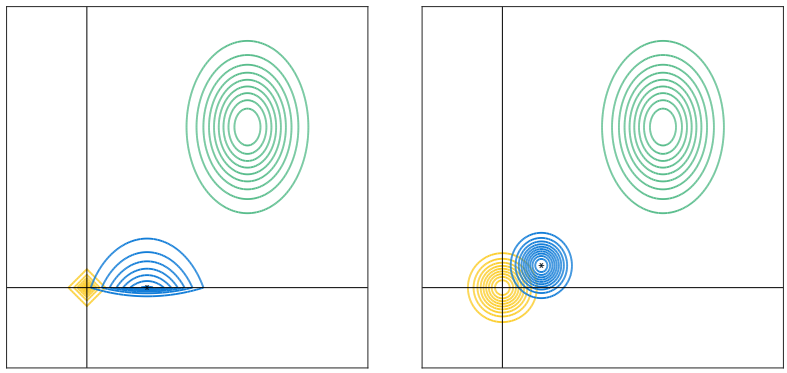

(a) (b)

Figure 3.2: Illustration of posterior with a: (a) ℓ_1 prior, and (b) Gaussian prior. Level sets of the likelihood (green), the prior (yellow) and the resulting posterior (blue). The markers indicate the corresponding maxima.

computation of the posterior density considerably, resulting in a posterior which is also a Gaussian distribution. Hence, the mean and covariance can be computed explicitly. Moreover, the computation of the posterior is easier when the forward model is linear.

Additionally, Gaussian prior densities can be used to approximate non-Gaussian prior densities when the observation of the variables is based on a sufficiently large number of mutually independent random events. For example, physical quantities that are expected to be the sum of many independent processes (such as measurement errors) often have distributions that are nearly normal. For an illustrative review of Gaussian priors, see [61].

3.1.2 Total variation prior

Originally introduced in image processing by Rudin, Osher and Fatemi in [11], the total variation (TV) regularizer reduces effectively the large spatial variations in a reconstructed image, whilst preserving sharp discontinuities (edges). Total variation regularization has been successfully applied to different imaging modalities where the exact reconstruction of feature edges is of superior importance. As for the case of EIT, TV regularization has been demonstrated as a very well suited regularization method for conductivities with piecewise regular sharp, well-defined edges [13, 15, 27–30, 61–63].

In a continuous formulation, the total variation of a function is defined by

$$\mathrm{TV}(f^\infty, \Omega) \quad := \quad sup \left\{ \int_\Omega f^\infty \nabla \cdot \mathrm{g} \, dx \mid \mathrm{g} \in C_c^1(\Omega, \mathbb{R}^n), \ \ |\mathrm{g}|_{L^\infty(\Omega)} \leq 1 \right\} \quad (3.5)$$

where $f^{\infty} \in L^1(\Omega)$ and $C_c^1(\Omega, \mathbb{R}^n)$ is the test function space consisting of continuously differentiable vector-valued functions with compact support contained in Ω. The *supremum norm* is denoted by $|\cdot|_{L^{\infty}(\Omega)}$. Restricting to the Sobolev space $W^{(1,1)}$ which is the function space such that the (weak) derivatives are in L^1 [64], the $TV(f^{\infty}, \Omega)$ becomes

$$\mathrm{TV}(f^{\infty}, \Omega) = \int_{\Omega} |\nabla f^{\infty}(\mathrm{x})| d\mathrm{x} \qquad f^{\infty} \in W^{(1,1)}, \tag{3.6}$$

Typically, $|\cdot|$ denotes the Euclidean norm, which leads to *isotropic* TV functional

$$\mathrm{TV}(f^{\infty}, \Omega) = \int_{\Omega} \sqrt{\sum_{i=1}^{n} \left(\frac{\partial f^{\infty}(\mathrm{x})}{\partial \mathrm{x}_i} \right)^2} d\mathrm{x} \tag{3.7}$$

If $|\cdot|$ represents the ℓ_1-norm in $\mathbb{R}^n$, then the *anisotropic* TV functional is obtained, i.e.

$$\mathrm{TV}(f^{\infty}, \Omega) = \int_{\Omega} \sum_{i=1}^{n} \left| \frac{\partial f^{\infty}(\mathrm{x})}{\partial \mathrm{x}_i} \right| d\mathrm{x}. \tag{3.8}$$

Employing either the isotropic or the anisotropic version of TV functionals has been demonstrated to yield sharp reconstructions. However, care has to be taken depending upon the prior information about the edge directions. In general, the isotropic TV functional would be a preferable choice if the edge direction is not available. On the contrary, the anisotropic TV functional can be a more suitable choice for the regularization, if the information exists. In Publication **II**, these differences are discussed.

For computational purposes, however, a discretized version of the TV functional has to be considered. In such a case, Equation (3.6), using the Euclidean norm, can be written as

$$\mathrm{TV}(f) = \sum_{i=1}^{m} \alpha_i \sqrt{\sum_{j=1}^{n} \left(\mathbf{D}_j f \right)_i^2}, \tag{3.9}$$

where the discrete differential operator corresponding to jth-coordinate direction is denoted by $\mathbf{D}_j$ and α_i is the regularization parameter. A differentiable version of Equation (3.9) can be obtained by adding a smoothing parameter $\beta > 0$ such as

$$\mathrm{TV}_{\beta}(f) = \sum_{i=1}^{m} \alpha_i \sqrt{\sum_{j=1}^{n} \left(\mathbf{D}_j f \right)_i^2 + \beta}, \tag{3.10}$$

On such an assumption, classical gradient based optimization methods can be applied to obtain the solution of the minimization problem. Hence, the isotropic formulation of the smoothed TV prior is given by

$$\pi_{prior}(f) \quad \propto \quad \exp\Big(- \sum_{i=1}^{m} \alpha_i \sqrt{\sum_{j=1}^{n} \left(\mathbf{D}_j f \right)_i^2 + \beta} \Big). \tag{3.11}$$

Similarly to (3.10), the anisotropic TV functional is given by

$$\mathrm{aTV}_\beta(f) = \sum_{i=1}^{m}\sum_{j=1}^{n} \alpha_i \left(\left(\mathbf{D}_j f\right)_i^2 + \beta \right)^{\frac{1}{2}}. \tag{3.12}$$

Hence, the smoothed TV prior employing the anisotropic form is defined as

$$\pi_{prior}(f) \quad \propto \quad \exp\left(- \sum_{i=1}^{m}\sum_{j=1}^{n} \alpha_i \left(\left(\mathbf{D}_j f\right)_i^2 + \beta \right)^{\frac{1}{2}} \right). \tag{3.13}$$

3.1.3 Extension of the TV functional to vector-valued parameters

Prior models based on the total variation functional can be extended to vector valued parameters in various ways. One option is to define the total variation regularization for these type of parameters by a component summation [65].

Formally, given a vector valued image $f^\infty \in S$ such that $S = \{f^\infty : R^n \to R^n\}$, the multi-dimensional TV functional is defined by

$$\mathrm{TV}_s(f^\infty, \Omega) := sup\left\{ \sum_{k=1}^{K} \int_\Omega f_k^\infty \nabla \cdot \mathrm{g}_k \, d\mathrm{x} \mid \mathrm{g}_k \in C_c^1\left(\Omega, \mathbb{R}^n \times \cdots \times \mathbb{R}^n\right), \right.$$
$$\left. |\mathrm{g}_k|_{L^\infty(\Omega)} \leq 1 \right\}, \tag{3.14}$$

which leads to

$$TV_s(f^\infty) = \sum_{k=1}^{K} \int_\Omega |\nabla f_k^\infty(x)| d\mathrm{x}. \tag{3.15}$$

Depending on the norm used in Equation (3.15), the anisotropic (ℓ_1-norm) or isotropic (Euclidean norm) formulation of the TV functional can be obtained.

Equation (3.15) may be the simplest way to define multidimensional TV. However, any information between components is neglected with this definition. This could lead to spatial and intensity shifts, as well as structure and scale changes, in different locations and orientation. One way to relate the components to each other is to consider certain features that vector valued functions may posses. These features can be spatial and intensity shifts, as well as structure and scale changes.

3.1.4 TV prior model augmented with cross gradient functional

The cross-gradient functional has been developed to relate similar spatial structures between the solutions of two models with different physical properties [66]. In this approach, two continuously differentiable functions $g(x)$ and $h(x)$ are considered locally structurally similar if the contour curves are parallel at each location x. The structural similarity can be determined by measuring the similarity of the gradient orientation, i.e. g(x) and h(x) are structurally similar if the

gradients of the functions are parallel. Hence, $\nabla g(x)$ and $\nabla h(x)$ are parallel at each point when

$$|\langle \nabla g(x), \nabla h(x) \rangle|^2 = \|\nabla g(x)\|^2 \|\nabla h(x)\|^2. \tag{3.16}$$

Therefore, the similarity of the orientation of the gradients of a two-valued-vector image can be measured by

$$R(g,h) = \int_\Omega \|\nabla g(x)\|^2 \|\nabla h(x)\|^2 - |\langle \nabla g(x), \nabla h(x) \rangle|^2 d\mathrm{x}. \tag{3.17}$$

Consequently, for a two-channel vector valued image

$$f \in \{f_1, f_2 \,|\, f_k \in \mathbb{R}^2, \text{ for } k = 1, 2\},$$

Equation (3.17) simplifies to

$$\begin{aligned} TVCG(f_1, f_2) &= \int_\Omega \|\nabla f_1\|^2 \|\nabla f_2\|^2 - |\langle \nabla f_1, \nabla f_2 \rangle|^2 d\mathrm{x} \\ &= \int_\Omega \|\nabla f_1\|^2 \|\nabla f_2\|^2 \sin^2(\vartheta) d\mathrm{x} \\ &= \int_\Omega \|\nabla f_1 \times \nabla f_2\|^2 d\mathrm{x}, \end{aligned} \tag{3.18}$$

where $\vartheta = \vartheta(x)$ is the angle between $\nabla f_1(x)$ and $\nabla f_2(x)$ in the plane containing them. Hence, (3.18) can be written in the discrete form as

$$\begin{aligned} TVCG(f_1, f_2) &= \sum_{i=1}^{m} \|(\mathbf{D} f_1 \times \mathbf{D} f_2)_i\|^2 \\ &= \sum_{i=1}^{m} \big((\mathbf{D}_x f_1)_i (\mathbf{D}_y f_2)_i - (\mathbf{D}_y f_1)_i (\mathbf{D}_x f_2)_i\big)^2. \end{aligned} \tag{3.19}$$

Henceforth, the functional consisting of the TV functional for f_1 and f_2 and augmented with the cross-gradient functional is given as

$$F(f_1, f_2) = TV_\beta(f_1) + TV_\beta(f_2) + \lambda\, CG(f_1, f_2), \tag{3.20}$$

where λ is a prior parameter which controls the degree of similarity between both components. Here, TV_β can be defined either as the isotropic or anisotropic formulation of the TV functional.

3.1.5 Joint total variation prior

Another generalization of the TV regularization to vector valued parameters has been proposed in [31]. In this approach, the total variation of a vector valued parameter is defined as the Euclidean norm of the vector of (scalar) total variations

of the components. Given a vector valued image $f^\infty \in S$, the multi-dimensional TV norm is written as

$$\mathrm{TV}_K(f^\infty) = \int_\Omega \sqrt{\sum_{k=1}^{K} \Big(|\nabla f_k^\infty(\mathrm{x})| \Big)^2} d\mathrm{x}, \quad \Omega \subseteq \{\mathbb{R}^n \times \cdots \times \mathbb{R}^n\}. \tag{3.21}$$

The above formulation of the multi-dimensional TV norm promotes sparsity on the gradient of each component of the image, while preserving rotationally invariant property in the spatial space.

In this thesis, a simplified version of Equation (3.21) is introduced. Here, a two-dimensional TV norm for a vector valued image with two components is considered. The TV-norm in this case is written as

$$\mathrm{TV}_2(f^\infty) = \int_\Omega \sqrt{\Big(|\nabla f_1^\infty(\mathrm{x})| \Big)^2 + \Big(|\nabla f_2^\infty(\mathrm{x})| \Big)^2} d\mathrm{x}, \tag{3.22}$$

where $\Omega \subseteq \{\mathbb{R}^2 \times \mathbb{R}^2\}$. Hence, the above equation may be written in the discrete form

$$\mathrm{TV}_{2,\beta}(f) = \sum_{i=1}^{m} \sqrt{\sum_{k=1}^{2} \left((\mathbf{D}_x\, f_k)_i^2 + (\mathbf{D}_y\, f_k)_i^2 \right) + \beta} \tag{3.23}$$

where β is added as a smoothing parameter to assure differentiability of the functional.

In the following, the functional (3.23) is refered as the smoothed *joint total variation* (JTV) of two channels. In accordance to the notation in [67], equation (3.23) is written as

$$\mathrm{TV}_{2,\beta}(f) = \mathrm{JTV}_\beta(f). \tag{3.24}$$

Further examples of other generalizations of the TV functional to vector valued images, which consider the inter-channel information, include the ones proposed by Sapiro and Ringach [32], and Kimmel, *et al.* [33].

3.2 POINT ESTIMATES OF THE TV POSTERIOR DISTRIBUTION IN EIT

The most popular point estimates encountered in the literature of statistical inverse problems are the *Maximum A Posteriori probability* (MAP) estimate and the *Conditional Mean* estimate. The MAP estimate is the (highest) mode of the posterior density and the CM estimate is the mean of the posterior density. In EIT inverse problem, such estimators can be written as

$$(\sigma_d, \varepsilon_d)_{\mathrm{CM}} = \int_{\mathbb{R}^{2n}} (\sigma_d, \varepsilon_d)\pi(\sigma_d, \varepsilon_d|U)d\Omega. \tag{3.25}$$

and

$$(\sigma_d, \varepsilon_d)_{\mathrm{MAP}} = \arg\max_{\sigma_d, \varepsilon_d} \{\pi(\sigma_d, \varepsilon_d|U)\} \tag{3.26}$$

where

$$\pi(\sigma_d, \varepsilon_d|U) = \pi_+(\sigma_d, \varepsilon_d) \exp\left(-\frac{1}{2}\|L_{\mathbf{e}}\left(\mathbf{U} - \mathrm{H}(\sigma_d, \varepsilon_d)\right)\|^2 - F(\sigma_d, \varepsilon_d)\right).$$

Here, the search for the conditional mean is an integration problem. In such case, the use of numerical quadrature methods would be unfeasible due to the large dimension of the parameter space in which the solution is defined. One way to compute the integral is to apply Monte Carlo (MC) integration. The MC integration consists of generating a representative ensemble of samples arrayed according to the distribution $\pi(\sigma_d, \varepsilon_d|U)$. To implement MC integration, we need to be able to produce such samples which requires the EIT forward problem to be evaluated several times. Hence, the computation time for determining the samples would be unpractical for higher dimensions.

In contrast, the computation of the MAP estimate leads typically to an optimization problem such as the weighted regularized least square (LS) problem:

$$\begin{aligned}(\sigma_d, \varepsilon_d)_{\mathrm{MAP}} &= \arg\min\Big\{\frac{1}{2}\|L_{\mathbf{e}}\left(\mathbf{U} - \mathrm{H}(\sigma_d, \varepsilon_d)\right)\|^2 \\ &\quad + F(\sigma_d, \varepsilon_d) + b(\sigma_d, \varepsilon_d)\Big\}, \end{aligned} \tag{3.27}$$

where the matrix $L_{\mathbf{e}}$ is the Cholesky factor of the inverse of the noise covariance matrix, ${\Gamma_{\mathbf{e}}}^{-1}$, $F(\sigma_d, \varepsilon_d)$ is the regularization functional, and $b(\sigma_d, \varepsilon_d)$ is the barrier function taking care of the positivity constraint.

This section describes the TV-type functionals $F(\sigma_d, \varepsilon_d)$ that were used in the computations of the MAP estimates in the EIT image reconstruction problem.

TV functional

We considered the isotropic total variation functional (3.10), which can be defined for the piecewise linear approximations (2.6) by

$$\mathrm{TV}_\beta(\sigma_d) = \sum_{i=1}^{N_2} \sqrt{(\mathbf{D}_x\, \sigma_d)_i^2 + (\mathbf{D}_y\, \sigma_d)_i^2 + \beta} \tag{3.28}$$

$$\mathrm{TV}_\beta(\varepsilon_d) = \sum_{i=1}^{N_2} \sqrt{(\mathbf{D}_x\, \varepsilon_d)_i^2 + (\mathbf{D}_y\, \varepsilon_d)_i^2 + \beta}. \tag{3.29}$$

N_2 is the number of elements in the mesh, $\mathbf{D}_x$ and $\mathbf{D}_y$ are the discrete differential operators corresponding to the x- and y-coordinate directions, in each of the mesh, and $\beta > 0$ is a parameter to ensures the differentiability of the TV functional. Hence, employing the functionals (3.28) and (3.29), the TV regularization functional becomes

$$F(\sigma_d, \varepsilon_d) = \alpha \mathrm{TV}_\beta(\sigma_d) + \varrho \mathrm{TV}_\beta(\varepsilon_d), \tag{3.30}$$

where $\alpha, \varrho > 0$ are the regularization parameters.

In Publication **I**, a systematic approach is introduced for the selection of the *prior parameter* in the TV functional. In such case, the prior parameter controls the weight of the prior model in the posterior estimates. Further examples for selecting α and ϱ include, the classical L-curve method [68], the Morozov discrepancy principle [69] or the modern learning based bi-level optimization approaches reported in [70, 71].

TV functional augmented with a cross-gradient functional

Using (3.20), the regularization functional consisting of the TV functional for σ_d and ε_d, augmented with the cross-gradient functional for promoting structural similarity of the unknown images becomes

$$F(\sigma_d, \varepsilon_d) = \alpha \mathrm{T}V_\beta(\sigma_d) + \varrho \mathrm{T}V_\beta(\varepsilon_d) + \lambda\, \mathrm{T}VCG(\sigma_d, \varepsilon_d), \tag{3.31}$$

where λ is a regularization parameter for the cross-gradient functional.

Joint total variation functional

The discrete approximation of the joint total variation function (3.23) for the parameter vectors σ_d and ε_d, is written as

$$\mathrm{J}TV_\beta(\sigma_d, \varepsilon_d) = \sum_{i=1}^{N_2} \sqrt{(\mathbf{D}_x\, \sigma_d)_i^2 + (\mathbf{D}_y\, \sigma_d)_i^2 + (\mathbf{D}_x\, \varepsilon_d)_i^2 + (\mathbf{D}_y\, \varepsilon_d)_i^2 + \beta}, \tag{3.32}$$

where N_2 denotes the number of elements in the FEM approximation. Hence, the regularization functional for the JTV regularization becomes

$$F(\sigma_d, \varepsilon_d) = \gamma\, \mathrm{J}TV_\beta(\sigma_d, \varepsilon_d), \tag{3.33}$$

where γ is the regularization parameter.

4 Review of results

In this chapter, a brief review of the results found in Publications I-III will be given.

4.1 PUBLICATION I: EXPERIMENTAL EVALUATION OF 3D ELECTRICAL IMPEDANCE TOMOGRAPHY WITH TOTAL VARIATION PRIOR

In this publication, a fully 3D EIT reconstruction approach for an absolute reconstruction, using the isotropic TV regularization (3.10), was developed. In this study, we concentrated on using methods that aided the reconstruction of only the real part of the admittivity (conductivity). The contributions of this study were two-folded: (i) it introduced a simple approach for the systematic selection of the prior parameter in the TV functional based on the *a priori* information of materials in the target, and their conductivity ranges, and (ii) it demonstrated, numerically, that absolute imaging, employing the TV prior in 3D EIT in a Bayesian framework with the systematic selection of the prior parameter, produces feasible reconstructions.

In this study, both synthetic EIT and laboratory EIT measurements were used in the numerical experiments. The synthetic EIT measurements were generated using the FE solver of the forward model. Details of the FE method employed in this study can be found in the original publication (I). The laboratory EIT measurements were carried out with the KIT4 measurement system developed at the Department of Applied Physics, University of Eastern Finland [72].

The results in this study demonstrated that employing a TV functional, with the proposed parameter selection, yields very robust 3D reconstructions of piecewise regular conductivities with sharp boundaries.

4.1.1 Methods

Measurement configuration

The numerical simulations and the real experiments were conducted using a cylindrical tank with a radius of 12.75 cm and a height of 20.4 cm. Sixty four equally spaced stainless steel electrodes were attached to the inner surface of the tank. The tank was filled with a saline solution, and plastic objects with different shapes were placed in it to form inhomogeneities to the conductivity distribution. The size of the electrodes was 4 cm $\times$ 4 cm. In this study, the current injection protocol used 16 injecting electrodes which is the number of the current injection channels limited by the hardware of our EIT system, see [72]. The currents were

injected between 60 different electrode pairs (1-5, 1-9, 1-13, ..., 1-64; 9-1, 9-5, 9-13..., 9-64; 52-1, 52-5, 52-9,..., 52-64; 60-1, 60-5, 60-9, ..., 60-64). The frequency of the current was 1 kHz and the amplitude was 1 mA. The voltages were measured against a ground electrode, which was always one of the current injection electrodes. The voltages between adjacent electrodes were calculated from these measurements. One measurement frame consisted of 3840 voltage readings.

In the case of the simulated voltages, gaussian noise was added. The noise consisted of two Gaussian components: one with a standard deviation of 1% of the level of each measurement, and one with 0.02% of the difference between the maximum and minimum values of voltage measurements.

Selection of the prior parameter

In the parameter selection strategy of the TV prior (3.11) proposed in Publication I, the conductivity σ was approximated in a piecewise linear basis, and the finite dimensional representation of the conductivity is given by $\sigma_d = [a_1, \ldots, a_{N_1}]^\top$, where $a_j > 0$ are the conductivity values in the nodes of the FE mesh. With this choice, the gradient of the piecewise linear approximation of σ_d is constant in each element Ω_i of the FE mesh, and the 2-norm of the gradient in Ω_i is of the form

$$g_i = \sqrt{(\mathbf{D}_x\, \sigma_d)_i^2 + (\mathbf{D}_y\, \sigma_d)_i^2 + (\mathbf{D}_z\, \sigma_d)_i^2}. \tag{4.1}$$

In the proposed approach, we assumed that the marginal (prior) probability density of g_i was given as

$$\pi(g_i) = \pi_+(g_i)\, c_i \exp\left(-\alpha_i g_i\right) \tag{4.2}$$

where π_+ is the positivity constraint function and $c_i, \alpha_i \in \mathbb{R}$ are parameters yet to be defined.

In order to set the TV prior parameters so that their (orders of) magnitudes roughly correspond to the expected conductivity ranges of the conductivity, we approximated that the gradient norms g_i, $i = 1, \ldots, N_2$ are mutually independent. Hence, the approximation for the prior density of g can be written as $\pi(g) \approx \prod_i \pi(g_i)$, and further by using (4.2)

$$\pi(g) \approx \prod_i \pi_+(g_i)\, c_i \exp\left(-\alpha_i g_i\right) \tag{4.3}$$

$$\approx C\, \pi_+(g)\, \exp\left(-\sum_i \alpha_i g_i\right), \tag{4.4}$$

where the constant is $C = \prod_i c_i$. Then, the prior density of σ_d is approximated as

$$\pi(\sigma_d) \propto \pi_+(\sigma_d)\, \pi_+(g)\, \exp\left(-\sum_i \alpha_i g_i\right). \tag{4.5}$$

For further details on the derivation of equation (4.5), we refer to appendix A1 of Publication **I**.

The selection of the parameters α_i in the TV functional (3.10) is based upon prior information regarding the range of conductivities within the object to be imaged. For this purpose, it is required that

$$P[g_i \geq 0] = \int_0^\infty \pi(g_i) dg_i = \int_0^\infty c_i \exp\left(-\alpha_i g_i\right) dg_i = 1 \tag{4.6}$$

where $P[\cdot]$ denotes the probability. Solving c_i from Equation (4.6) yields $c_i = \alpha_i$. Given $g_{\max,i}$, the estimate for maximum of the gradient norm g_i, the confidence interval $(0, g_{\max,i})$ for the gradient norms g_i with confidence coefficient $p\%$ is computed as

$$P[0 \leq g_i \leq g_{\max,i}] = \int_0^{g_{\max,i}} \alpha_i \exp\left(-\alpha_i g_i\right) dg_i = \frac{p}{100}, \tag{4.7}$$

from which the parameter α_i can be obtained by

$$\alpha_i = -\frac{\ln\left(1 - \frac{p}{100}\right)}{g_{\max,i}}. \tag{4.8}$$

In this approach, the choice $g_{\max,i}$ depends on the discretization of the conductivity distribution σ. In the case the conductivity is approximated in a piecewise linear basis utilizing a tetrahedral FE mesh, $g_{\max,i}$ that can be approximated by

$$g_{\max,i} = \frac{\sigma_{\max} - \sigma_{\min}}{d_i} \tag{4.9}$$

where $\sigma_{\min}$ and $\sigma_{\max}$, respectively, are the expected minimum and maximum conductivity within the object Ω, and d_i is the mean edge length in the mesh element Ω_i. Further, if the FE mesh is approximately uniform, one can choose $d_i = d$ for all i, where d is the mean edge length over the entire FE mesh. In such a case, Equations (4.8 and 4.9) are written as

$$\alpha_{sys} = -\frac{\ln\left(1 - \frac{p}{100}\right)}{g_{\max}} \quad \text{where} \quad g_{\max} = \frac{\sigma_{\max} - \sigma_{\min}}{d}. \tag{4.10}$$

4.1.2 Results

Numerical experiments using simulated data

To study the proposed parameter selection strategy, we computed relative L_2-errors (RE) and errors using the bounded variation norm (BV-norm) of the reconstructed conductivity distributions for different values of the TV prior parameter α. The range of values employed for α was 10^{-3} to 10^3. The relative L_2-errors between the true conductivity and the reconstruction were computed as

$$RE = \frac{\|P\sigma_{\text{true}} - \sigma_{\text{MAP}}\|_2}{\|P\sigma_{\text{true}}\|_2}, \tag{4.11}$$

where P is a matrix that interpolates the nodal conductivity in a dense FE mesh into a nodal conductivity in a coarse FE mesh. Both FEs employed first order basis functions. For computing the errors using the BV-norm, we defined the BV-norm as

$$\|u\|_{BV} = \|u\|_1 + \mathrm{TV}_\beta(u), \tag{4.12}$$

where TV_β is the smoothed isotropic TV functional (3.10). Hence, the errors using the BV-norm were computed using

$$\varepsilon_{BV} = \|P\sigma_{\text{true}} - \sigma_{\text{MAP}}\|_{BV}. \tag{4.13}$$

The errors were calculated for reconstructions corresponding to three realizations of the simulated EIT measurements.

The simulated test cases were focused in evaluating the performance of the proposed parameter choice of the 3D TV prior. For that purpose, we considered three realizations of noise and computed relative L_2-errors (4.11) and errors using the BV-Norm (4.15).

The relative errors of reconstructed conductivity distributions, corresponding to a range of values of α, are plotted in Figure 4.1 using the logarithmic scale. In this figure, three values of α are highlighted: the systematically selected prior parameter $\alpha_{\text{sys}} = 0.742$, $\alpha^1_{\text{opt}} = 0.091$ and $\alpha^{2,3}_{\text{opt}} = 0.069$ which are the values of α, corresponding to the minimum in the relative reconstruction error (4.11), for each realization of the noise.

The errors using the BV-Norm are shown in Figure 4.2. In this figure, four values of α are highlighted. The systematically selected prior parameter $\alpha_{\text{sys}} = 0.742$, $\alpha^{1,3}_{\text{opt}} = 0.160$, and $\alpha^2_{\text{opt}} = 0.121$, which correspond to the minimum in the reconstruction error using (4.15) for each of the three realizations of the data.

From figures 4.1 and 4.2, one can see that the systematic parameter α_{sys} is closer to the optimal value α_{opt}, when the reconstruction error is measured using the BV-norm, instead of the relative L_2-error. In Figure 4.1 (the relative L_2-error), the mean of the distance $|\alpha_{sys} - \alpha_{opt}|$ is 0.666 and in Figure 4.2 (the BV-norm) the mean distance is 0.595.

The reconstructions using α_{sys} and α_{opt} are shown in Figure 4.3. In both of the estimates, the conductivity of the inclusion and background are also close to the true values. Moreover, the reconstructed inclusion is in the correct location and resembles, in shape, the true simulated target.

Real measurement data

To evaluate the TV prior in a 3D EIT setting, laboratory experiments using real experimental measurement data were carried out. The experiments comprised of six test cases. Each test case used plastic objects with different shapes to create inhomogeneities in the resulting conductivity distributions.

In one of the test cases (Figure 4.4), feasible estimates for the locations, shapes and sizes of the plastic inclusions were obtained. In this case, conductivity estimates of the (non-conductive) plastic inclusions were close to zero. Visible small

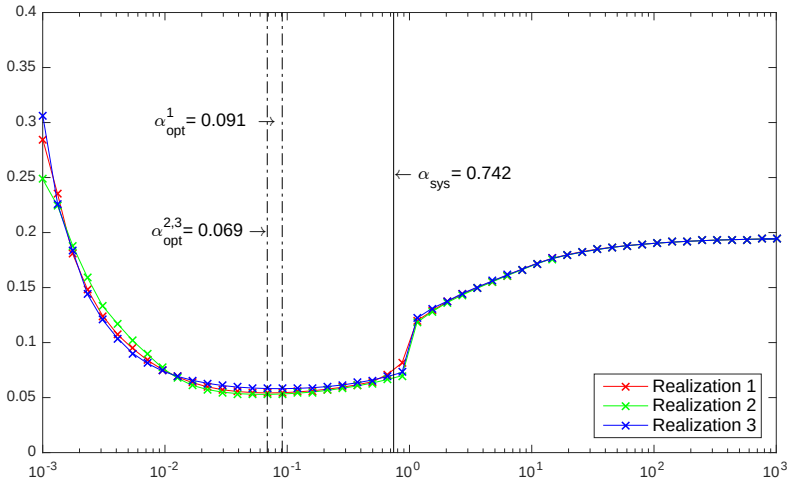

Figure 4.1: The relative errors (4.11) for a range of regularization parameter values α. The relative errors are shown for three different realizations of the measurement noise. The values giving the smallest relative error for each realization of noise are denoted by α^{i}_{opt} where the superscript i refers to the realization. The systematically selected parameter is denoted by α_{sys}.

artifacts near the boundary of the tank can be seen in the reconstructions. For example, in the horizontal cross-section of the reconstructions, the artifacts were located near the position of the electrodes. These types of artifacts arise due to modeling errors such as (small) inaccuracies in the electrode locations and discretization accuracies in the FE model.

4.1.3 Conclusions

Our findings in Publication I demonstrated the feasibility of the TV prior in 3D EIT, using experimental measurement data from target conductivities that can not be handled by either 2D or 2.5D models. Moreover, the results in figures (4.4) described in this section, together with results displayed in Figure 5, 6, and 7 in Publication I, show that the use of the 3D TV prior improves the quality of 3D EIT reconstructions compared to the reconstructions using a standard Gaussian smoothness prior. Furthermore, results in Figure 4.1 and 4.2 support that the proposed selection of the prior parameter provides similar reconstructions to the optimal value despite of being based on approximations. This can be of significant advantage in the practical applications since the method only requires approximate knowledge of the range of conductivities in the target for the computation of the prior parameter, and such information is generally available.

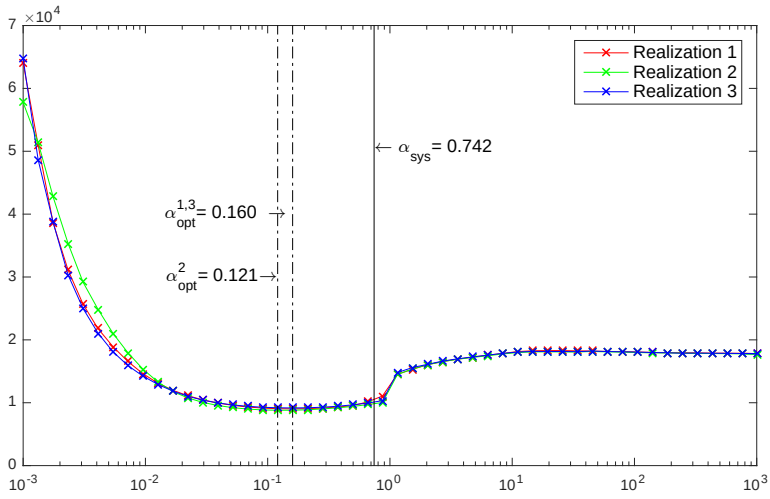

Figure 4.2: The errors (4.15) for a range of regularization parameter values α. The systematically selected parameter is denoted by α_{sys} The relative errors are shown for three different realizations of the measurement noise. The values giving the smallest relative error for each realization of noise are denoted by α^1_{opt}, α^2_{opt} and α^3_{opt}.

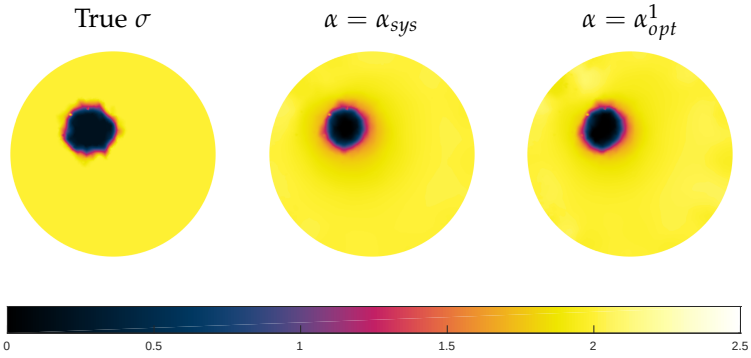

Figure 4.3: These cross-sectional slices of EIT reconstructions corresponding to the parameter values α_{sys} and α_{opt} (the BV-norm, the 1st realization).

4.2 PUBLICATION II: ISOTROPIC AND ANISOTROPIC TOTAL VARIATION REGULARIZATION IN ELECTRICAL IMPEDANCE TOMOGRAPHY

In Publication II, we investigated the effects of both isotropic (3.10) and anisotropic (3.12) TV regularizations on EIT. A characteristic difference between these two

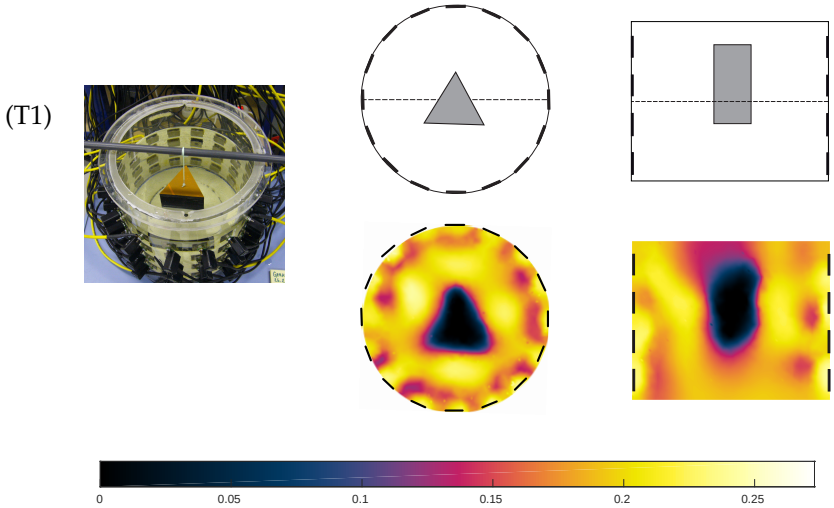

Figure 4.4: The estimated conductivity distributions based on experiments: a resistive triangular-shape-prism inclusion of 10.4 cm height and located 6 cm from the bottom of the tank. A photograph of the measurement tank at the initial state is shown in the first column. Indicative schematics of both the transverse and longitudinal cross-sections are shown in the first row of the second column. Transverse cross-sections are shown on the top row of the two right hand side columns with the corresponding longitudinal cross-sections of the reconstructions on the row directly below.

particular forms of the TV regularization is that the isotropic TV is rotationally invariant, whereas the anisotropic TV is not. In EIT, the information on the fine details of edges contained in the measurements is limited, and it opens the question of how large an impact, the selection of the TV regularization variant, has upon the reconstructed images. The results in this research article demonstrated that the choice between isotropic and anisotropic TV regularization has a significant impact on the properties of EIT reconstructions. In this work, the effect in the EIT reconstructions of both forms of the TV regularizer was investigated based on a set of real measurements.

4.2.1 Methods

Measurement configuration

The EIT measurements were carried out with the KIT4 measurement system. The experiments were carried out using a cylindrical tank with a diameter of 28.0 cm and a height of 7.0 cm. Sixteen equally spaced stainless steel electrodes (width 2.5 cm, height 7.0 cm) were attached to the inner surface of the tank. The currents were injected such that electrode 1 was fixed as the sink electrode, and then ap-

plying pairwise currents, sequentially, between the sink electrode and each of the 15 remaining electrodes. Corresponding to each current injection, the potentials on all of the 15 remaining electrodes were measured against the sink electrode, which itself, was connected to the common ground. The frequency of the current was 1 kHz and the amplitude was 1 mA. With this measurement protocol, one measurement frame consisted of 225 voltage readings (i.e., $V \in \mathbb{R}^{225}$).

The tank was filled with saline solution, and translationally symmetric plastic objects, with different shapes, were placed in the tank, in order to form inhomogeneities in the conductivity distribution.

4.2.2 Results

An example of the results is shown in Figure 4.5. In this figure, the image on the left shows a photograph of the true target, which included a triangular prism. The reconstructions with the isotropic (3.10) and anisotropic (3.12) TV regularizations are shown in the middle and the right of the figure, respectively. Here, α and β were selected as $\alpha = \alpha_{sys}$, $\beta = 10^{-3}$. The conductivity in this case was represented in a piecewise linear basis.

In both reconstructions, the inclusion has sharp edges and is located approximately at the same position as the true object. The reconstruction employing the isotropic form resembles the triangular shape of the inclusion, whereas in the case of the anisotropic form, the shape deviates from the real shape. In this reconstruction, the edges of the inclusion are aligned with the co-ordinate axes.

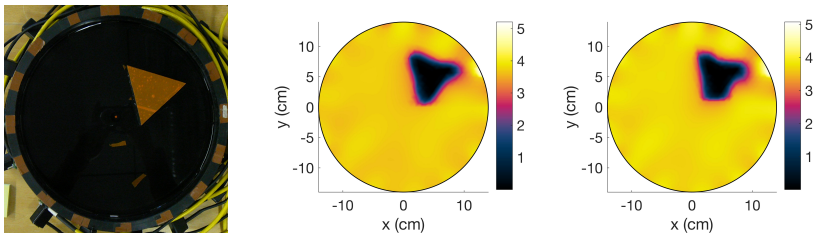

Figure 4.5: Results with piecewise linear discretization for the conductivity and systematically selected α. Left: photograph of the target; middle: reconstruction based on the isotropic TV prior; right: reconstruction based on the anisotropic TV prior.

In Figure 4.6, the results demonstrate the robustness of the reconstructions employing the isotropic TV regularization, with respect to the choice of α and β. This figure comprises reconstructions of the conductivity with choices of α varying from $10^{-1}\alpha_{sys}$ to $10\alpha_{sys}$ and β varying from 10^{-3} to 10^{-1}. As it can be seen from Figure 4.6, a triangular shaped inclusion can be recovered with various choices of α and β. In these reconstructions, the sharpness of the boundaries decreases as the value of β goes higher. Moreover, the reconstructions feature sev-

eral artifacts with the smallest value of α, as can be expected in under-regularized solutions.

The reconstructions with the anisotropic TV functional in Figure 4.7 are in good correspondence with the above results. The reconstructions employing the anisotropic TV are satisfactory when the choices of α ranged between $10^{-1}\alpha_{sys}$ to $10^{2}\alpha_{sys}$ and β between 10^{-4} to 10^{-1}. The rest of the computed reconstructions presented artifacts. Most importantly, all these images exhibited a blocky inclusion which resembles the shape of a triangle.

4.2.3 Conclusions

In this publication, a study of the performance of isotropic and anisotropic TV regularizations on EIT was conducted. To study the dependence of the solutions on the regularization parameter α, and the smoothing parameter β, reconstructions were derived using real measurements. Our findings were consistent and showed that, in feasible ranges of the parameters α and β, reasonable reconstructions are achievable. In the case of reconstructions utilizing the anisotropic TV form, however, the inclusion boundaries tend to align along the co-ordinate axes. This geometric distortion caused by the anisotropic TV regularization, is a well-known phenomenon in other applications. The results in this study demonstrate that in EIT, the magnitude of this geometric distortion is remarkably large.

4.3 PUBLICATION III: JOINT RECONSTRUCTION OF CONDUCTIVITY AND PERMITTIVITY IN EIT USING STRUCTURAL SIMILARITY PRIORS

In Publication III, we studied two prior models, namely the TV functional augmented with either a cross-gradient (CG) functional and a joint total variation (JTV) functional. These priors promote the spatial similarities between two unknown parameters. We utilized such priors for the joint estimation of the conductivity and permittivity in a complex valued EIT problem. In order to assess the quality of the conductivity and permittivity estimates, we computed three fidelity measures i) the L_2 relative error, ii) the BV-norm error and iii) the structural similarity index (SSIM), see [73]. The reconstructions utilizing the TVCG and JTV priors were compared with the ones using an isotropic TV functional.

4.3.1 Methods

Fidelity measures

The performance of the proposed regularization methods for the joint reconstruction of the conductivity and permittivity was evaluated with three fidelity measures. Firstly, relative L_2 – errors between the true target distributions and their reconstructions were computed. The relative error for conductivity was calculated

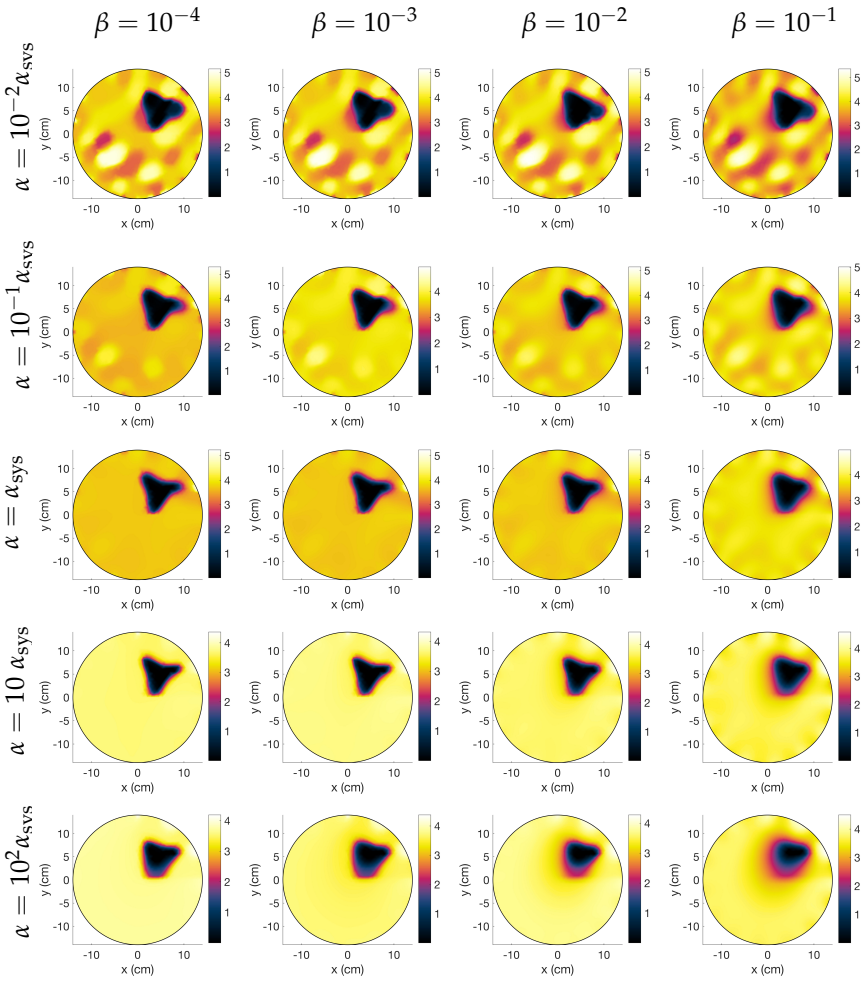

Figure 4.6: Results based on the isotropic TV prior and piecewise linear discretization for the conductivity. The table shows the EIT reconstructions corresponding to twenty combinations of α and β. Parameter α increases from top to bottom (values shown on far left), and β increases from left to right (values shown on top of the respective columns).

as

$$\mathrm{RE}(\sigma_d) = \frac{\|P\sigma_{\text{true}} - \sigma_d\|_2}{\|P\sigma_{\text{true}}\|_2} \cdot 100(\%). \tag{4.14}$$

where P is a matrix which interpolates the nodal conductivity in $\mathcal{M}_0^{1st}$ into a nodal conductivity in $\mathcal{M}_1^{1st}$. The relative error of the permittivity $\mathrm{RE}(\varepsilon_d)$ was

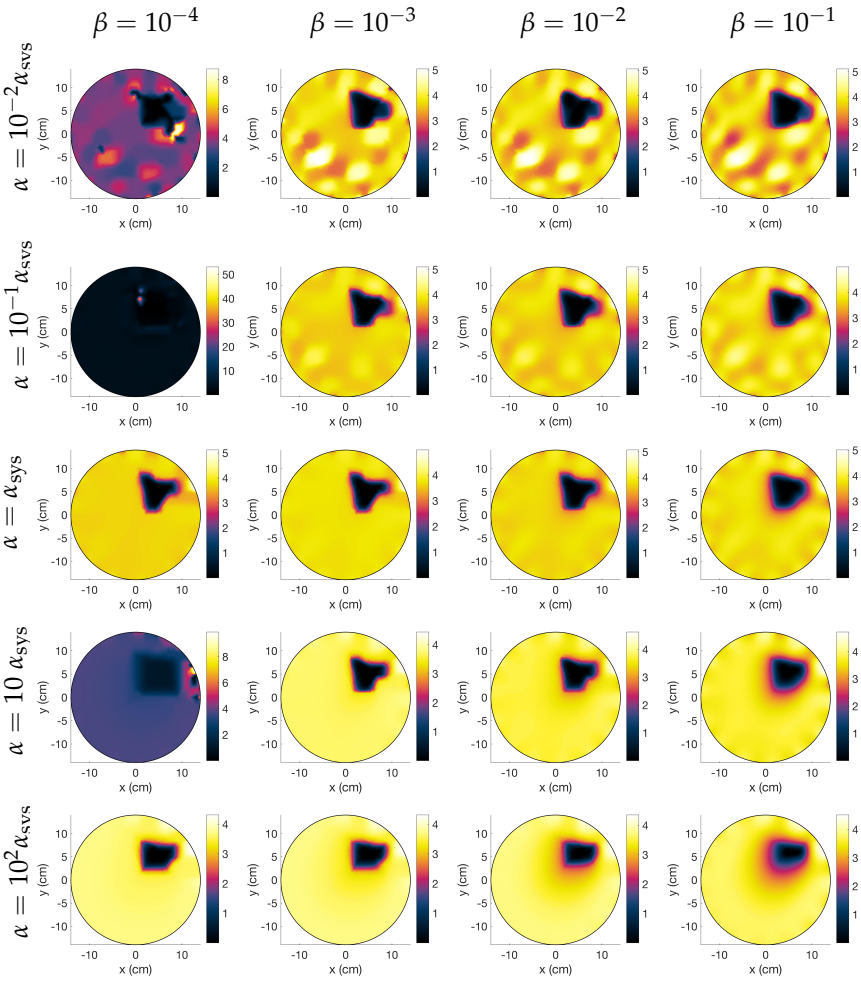

Figure 4.7: Results based on the anisotropic TV prior and piecewise linear discretization for the conductivity. The table shows the EIT reconstructions corresponding to twenty combinations of α and β. Parameter α increases from top to bottom (values shown on the far left), and β increases from left to right (values shown on top of the respective columns).

calculated similarly.

The second fidelity measure was the bounded variation norm (BV-norm) of the error, defined for the conductivity as

$$\mathrm{BVE}(\sigma_d) = \log\left(\|P\sigma_{\mathrm{true}} - \sigma_d\|_1 + \mathrm{TV}_\beta(P\sigma_{\mathrm{true}} - \sigma_d)\right). \tag{4.15}$$

The $\mathrm{BVE}(\varepsilon_d)$ was calculated similarly.

The third fidelity measure considered in this study was the structural similarity (SSIM) index, which is a measurement that has been developed for quantifying the perceptual similarity of two images [73]. The SSIM index is a decimal value between 0 and 1, where the value 1 is only reachable in the case when two images are identical. For further details on the SSIM index, see [73]. The following SSIM indexes were computed: (i) SSIM($\sigma_{\text{true}}, \sigma_d$), (ii) SSIM($\varepsilon_{\text{true}}, \varepsilon_d$), (iii) SSIM($\nabla\sigma_{\text{true}}, \nabla\sigma_d$), (iv) SSIM($\nabla\varepsilon_{\text{true}}, \nabla\varepsilon_d$) and (v) SSIM($\sigma_d, \varepsilon_d$).

Reconstruction methods and regularization parameters

The following reconstructions were considered in the results section:

(TV) The solution of (3.27) with the total variation regularization (3.30). The regularization parameters (α, ϱ) were selected by finding the combination of values which minimizes RE$((\sigma_d, \varepsilon_d)^\top)$.

(TV+CG) The solution of (3.27) with the total variation augmented with cross-gradient regularization (3.31). The values of (α, ϱ) were fixed to the same as those used for the TV regularization. The value of λ in (3.20) was selected by a one-dimensional search, finding a value that leads to the structurally most similar estimates of the conductivity and permittivity, with respect the true target distributions, where the value of λ maximizes SSIM$(\theta_{\text{true}}, \hat{\theta})$ where $\theta_{\text{true}} = (\sigma_{\text{true}}, \varepsilon_{\text{true}})^\top$ and $\hat{\theta} = (\sigma_d, \varepsilon_d)^\top$.

(JTV) The solution of (3.27) with the joint total variation regularization (3.33). The regularization parameter γ was selected by finding a value which minimizes RE$((\sigma_d, \varepsilon_d)^\top)$.

Simulation of the measurement data

Two computational domains were considered in the simulation of the measurements: an idealized cross-section of a human thorax and a circular domain with radius $r = 12.75$ cm. The measurement setup consisted of 16 equally spaced electrodes. Currents were selected such that one electrode was fixed as the sink electrode to each one of the 15 remaining electrodes. The same process was repeated using electrodes {1, 5, 9, 13 } as the sink, leading to a total of 60 pairwise current injections and 900 voltage measurements. The frequency of the injected currents was set to 100 Hz and the amplitude was set to 1 mA. Then, EIT measurements were generated using the FE solver used in the forward model. For further details regarding the simulation of the measurement data, see the original publication.

4.3.2 Results

2D simulation of circular domain

The target conductivity and permittivity, together with their gradients, are shown in the top row of Figure 4.8. TV reconstructions are shown in row 2. The reconstructions with the TV+CG funcitonal and the JTV functional are shown in the third and fourth rows, respectively.

As can be seen from the figure, both of the structural similarity priors (the TV+CG and JTV) improved the estimates over the ones using the TV functional, in the case where σ and ε were structurally similar. The fidelity measures are given in Table 4.1.

Comparisons between TV and TV+CG estimates revealed that TV+CG performed better in terms of the SSIM, which measures the structural similarity of the reconstruction and the true unknown. The estimates σ_d and ε_d also had more uniform quality, in terms of fidelity values. Some of the relative and BVN errors for the TV+CG were slightly larger than those for TV; this feature can be attributed to the poorer contrast of the inclusion in the TV+CG reconstructions, and in the case of the BV-Norm measure to the small smoothing of the estimates caused by the cross-gradient term.

Based on all the fidelity measures against the true target distributions, the JTV functional produces the most accurate estimates compared to the true targets, with respect all of the fidelity measures. However, based on visual interpretation, the TV+CG has higher structural similarity *b*etween the estimates $\hat{\sigma}_d$ and $\hat{\varepsilon}_d$) than the ones obtained with JTV. This interpretation is also reflected in the structural similarity index $SSIM(\hat{\sigma}_d, \hat{\varepsilon}_d)$. In this case, the value of $SSIM(\hat{\sigma}_d, \hat{\varepsilon}_d)$, when TV+CG prior was employed, was bigger than the structural similarity value obtained with JTV.

Table 4.1: The fidelity measures for the circular mesh case in Figure 4.8.

	Circular Mesh		
	TV	TV + CG	JTV
$RE(\hat{\sigma}_d)$	10.843 %	19.264 %	8.661 %
$RE(\hat{\varepsilon}_d)$	15.782 %	31.082 %	14.401 %
$SSIM(\hat{\sigma}_d, \sigma_{true})$	0.914	0.846	0.927
$SSIM(\hat{\varepsilon}_d, \varepsilon_{true})$	0.917	0.845	0.915
$SSIM(\hat{\sigma}_d, \hat{\varepsilon}_d)$	0.598	0.614	0.611
$BV - Norm(\hat{\sigma}_d)$	4.675	5.037	4.572
$BV - Norm(\hat{\varepsilon}_d)$	4.410	4.841	4.395

2D simulation of imaging the thorax

In Figure 4.9, the target conductivity and permittivity of an idealized 2D human thorax phantom, together with respective reconstructions, are shown. The values for the conductivity and permittivity in the different regions of the true target

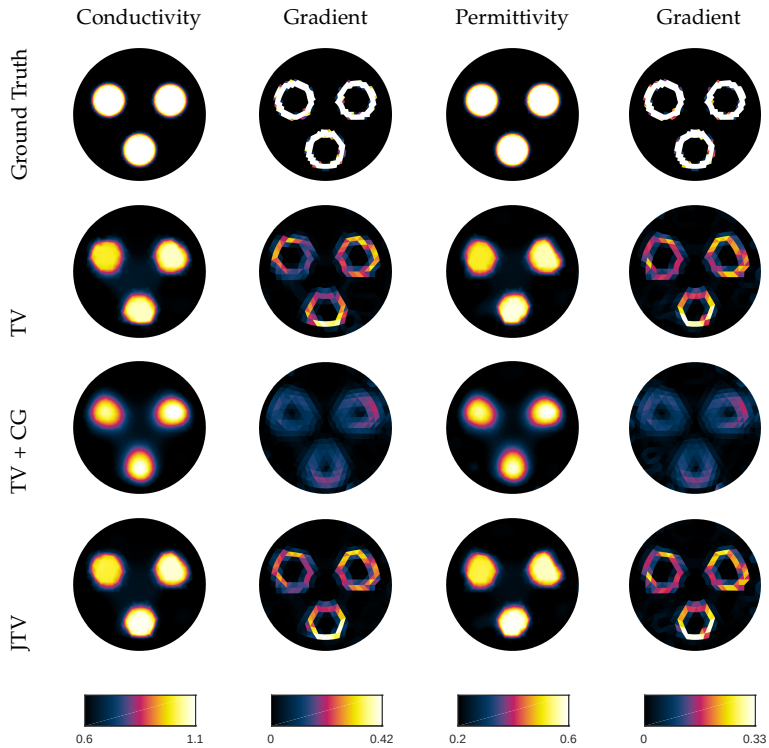

Figure 4.8: Reconstructions from simulated EIT data of 2D circular model. Columns 1 and 3 show conductivity σ and permittivity ε. Columns 2 and 4 show the gradients $|\nabla\sigma|$ and $|\nabla\varepsilon|$, respectively.

distributions are listed in Table 4.2. Reconstructions employing the TV functional, the TV+CG reconstructions, and the JTV reconstructions are shown in rows 2,3 and 4, respectively. The fidelity measures are given in Table 4.3.

The JTV and the TV+CG again display a clear improvement over the TV functional. The estimates with both the JTV and the TV+CG are quite similar to each other, but with some of the fidelity measures favoring one method over the other, and *vice versa*.

Table 4.2: Admittivity values for the simulated thorax phantom with heart and lungs [74]. These values represent a rough average of conductivity and permittivity in fat tissue in chest, heart and lungs.

	Admittivity
Lungs	$0.50 + \mathrm{i}\,\omega\, 0.20$ S/m
Heart	$1.10 + \mathrm{i}\,\omega\, 0.60$ S/m
Background	$0.80 + \mathrm{i}\,\omega\, 0.40$ S/m

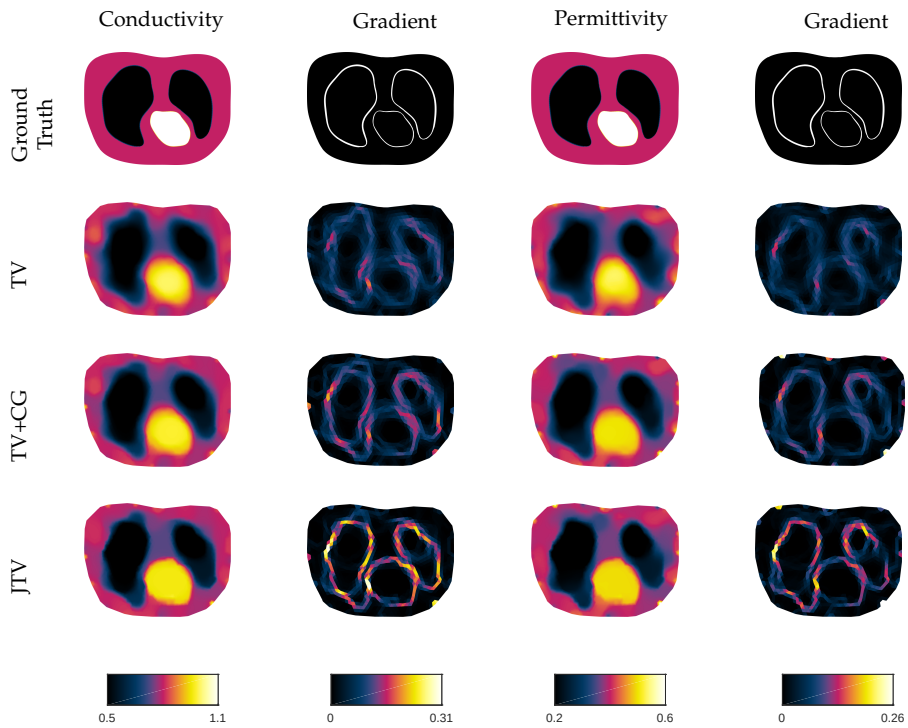

Figure 4.9: Reconstructions from simulated EIT data of 2D thorax model. Columns 1 and 3 show conductivity σ and permittivity ε. Columns 2 and 4 show the gradients $|\nabla\sigma|$ and $|\nabla\varepsilon|$, respectively.

Table 4.3: The fidelity measures for the 2D thorax mesh case in Figure 4.9.

	Anatomical Mesh		
	TV	TV + CG	JTV
$RE(\hat{\sigma}_d)$	39.83 %	38.95 %	36.45 %
$RE(\hat{\varepsilon}_d)$	43.24 %	45.62 %	40.62 %
$SSIM(\hat{\sigma}_d, \sigma_{true})$	0.7758	0.7845	0.8065
$SSIM(\hat{\varepsilon}_d, \varepsilon_{true})$	0.7852	0.7866	0.7987
$SSIM(\hat{\sigma}_d, \hat{\varepsilon}_d)$	0.6986	0.7029	0.6959
$BV - Norm(\hat{\sigma}_d)$	6.9843	6.9551	6.9071
$BV - Norm(\hat{\varepsilon}_d)$	6.7204	6.7209	6.6707

4.3.3 Conclusions

In this study, two joint reconstructing methods, of the conductivity and permittivity distributions based on complex valued EIT data, were proposed. The two methods consisted of: (i) augmenting conventional total variation (TV) functional

with a cross-gradient functional for promoting structural similarities between the conductivity and permittivity distribution and (ii) the joint total variation (JTV) functional. The approaches were tested using simulated EIT data and compared to reconstructions using the TV functional. Both of the approaches were found to improve the estimates in terms of structural similarity between the estimates and the true target distributions. The JTV regularization approach gave the best results in terms of fidelity measures, and turned out to be a highly feasible regularization method for use in the joint reconstruction of conductivity and permittivity, in cases when the unknowns can be expected to be structurally similar.

In summary, the results demonstrated that using the structural information in the reconstruction methods could lead to sharper images with less artifacts and more accurate representations of internal boundaries, than the conventional methods such as the TV regularization.

5 Summary and conclusions

Recently, there have been new developments in the use of the TV functional. Some have extended the applicabilities the TV functional to vector-valued images, whilst others improve the contrast, ameliorate the stair–casing effect, or preserve other fine scale image features, such as textures. The TV functional penalizes highly oscillating patterns in the reconstructed image, noise in particular, while preserving sharp transitions such as edges. This feature has been advantageous for the development of reconstruction methods in EIT.

In this work, the main emphasis was to study prior models based on sparsity–promoting TV functionals in EIT. In general, the underlying principle of these functionals is that an admittivity parameter, with excessive and possible spurious "details", has a corresponding high total variation. According to this principle, minimizing the total variation of such a parameter, subject to it being a close match to the original admittivity, removes unwanted details, while promoting sharp variations in the recovered parameter. The use of these priors improves the reliability of the reconstructions of piecewise regular admittivity distributions. The performance of the reconstruction schemes employing the proposed priors were evaluated using both simulated and experimental data. The effects of the proposed priors on EIT reconstructions were investigated in three studies.

In Publication **I**, we developed a fully 3D EIT approach for reconstructing piecewise regular conductivities with TV regularization. In this study, a systematic selection of the prior parameter in the TV functional was also introduced. This choice was based on *a priori* information of the range of conductivity values of the target. It was demonstrated that the proposed choice yields parameter values which lead to reconstructions that are similar to the ones using an optimal value of the prior parameter. Additionally, the feasibility of the TV prior in 3D EIT was studied and evaluated using experimental measurement data. Our findings demonstrated that the proposed parameter selection strategy yields sharp reconstructions in 3D EIT.

In Publication **II**, we investigated the performance of isotropic and anisotropic TV regularization in EIT. For this purpose, the two TV regularization schemes were compared based on a set of experiments made in the laboratory. The dependence of the solutions on the regularization parameter α, smoothing parameter β and discretization of the conductivity was studied in these experiments. Results verified that in the feasible ranges of parameters α and β, the use of the isotropic form of TV lead to feasible EIT reconstructions. Whereas the anisotropic form caused distortions by aligning the boundaries of the inclusions to the co–ordinates axes in the entire range of the tested parameters.

In Publication **III**, two joint prior models were investigated in the context of

the image reconstruction problem in EIT. These priors were based on generalizations of the TV functional. Their main characteristic was to promote mutual spatial similarities between the conductivity and permittivity. The performance of reconstruction schemes employing these priors was tested with simulated EIT data. The reconstructions were compared with the ones employing a TV prior for the conductivity and permittivity. The numerical results indicated that exploiting the mutual structural information improved significantly the quality of the reconstructions in the areas where common spatial similarities were shared. Further, the numerical results show that including the mutual structural information of the conductivity and permittivity in the reconstructions schemes leads to sharper reconstructions, with less artifacts, and more accurate representation of internal boundaries.

To conclude, the joint prior models such as the ones presented in this study provide appropriate tools to link the conductivity and permittivity distribution in the reconstruction scheme. Thus, the applicability of our approach may include other tomography modalities which handle coupled vector-valued images.

BIBLIOGRAPHY

[1] A. R. Ruuskanen, A. Seppänen, S. Duncan, E. Somersalo, and J. P. Kaipio, "Using process tomography as a sensor for optimal control," *Applied Numerical Mathematics* **56**, 37–54 (2006).

[2] V. Cherepenin, A. Karpov, A. Korjenevsky, V. Kornienko, A. Mazaletskaya, D. Mazourov, and D. Meister, "A 3D electrical impedance tomography (EIT) system for breast cancer detection," *Physiological Measurement* **22**, 9 (2001).

[3] I. Frerichs, "Electrical impedance tomography (EIT) in applications related to lung and ventilation: a review of experimental and clinical activities," *Physiological Measurement* **21**, R1 (2000).

[4] T. Tidswell, A. Gibson, R. Bayford, and D. Holder, "Three-dimensional electrical impedance tomography of human brain activity," *NeuroImage* **13**, 283–294 (2001).

[5] A. Romsauerova, A. McEwan, L. Horesh, R. Yerworth, R. Bayford, and D. S. Holder, "Multi-frequency electrical impedance tomography (EIT) of the adult human head: initial findings in brain tumours, arteriovenous malformations and chronic stroke, development of an analysis method and calibration," *Physiological Measurement* **27**, S147 (2006).

[6] A. Ramirez, W. Daily, A. Binley, D. LaBrecque, and D. Roelant, "Detection of Leaks in Underground Storage Tanks Using Electrical Resistance Methods," *Journal of Environmental and Engineering Geophysics* **1**, 189–203 (1996).

[7] K. Karhunen, A. Seppänen, A. Lehikoinen, J. Blunt, J. P. Kaipio, and P. J. M. Monteiro, "Electrical resistance tomography imaging of concrete.," *Cement and Concrete Research* **40**, 137–145 (2010).

[8] D. Barber and B. Brown, "Applied potential tomography," *Journal of physics. E. Scientific instruments* **17**, 723–733 (1984).

[9] J. P. Kaipio and E. Somersalo, *Statistical and Computational Inverse Problems* (New York: Springer, 2004).

[10] A. Tarantola, *Inverse problem theory and methods for model parameter estimation* (SIAM, 2005).

[11] L. I. Rudin, S. Osher, and E. Fatemi, "Nonlinear total variation based noise removal algorithms.," *Physica D.* **60**, 259–268 (1992).

[12] D. C. Dobson and F. Santosa, "An image-enhancement technique for electrical impedance tomography," *Inverse Problems* **10**, 317 (1994).

[13] D. C. Dobson, "Recovery of blocky images in electrical impedance tomography," in *Inverse Problems in Medical Imaging and Nondestructive Testing* (Springer, 1997), pp. 43–64.

[14] B. Jin, T. Khan, and P. Maass, "A reconstruction algorithm for electrical impedance tomography based on sparsity regularization," *International Journal for Numerical Methods in Engineering* **89**, 337–353 (2012).

[15] M. Gehre, T. Kluth, A. Lipponen, B. Jin, A. Seppänen, J. P. Kaipio, and P. Maass, "Sparsity reconstruction in electrical impedance tomography: an experimental evaluation," *Journal of Computational and Applied Mathematics* **236**, 2126–2136 (2012).

[16] Z. Fan and R. X. Gao, "An adaptive total variation regularization method for electrical capacitance tomography," in *Instrumentation and Measurement Technology Conference (I2MTC), 2012 IEEE International* (IEEE, 2012), pp. 2230–2235.

[17] M. Soleimani and W. Lionheart, "Nonlinear image reconstruction for electrical capacitance tomography using experimental data," *Measurement Science and Technology* **16**, 1987 (2005).

[18] H. Wang, I. Fedchenia, S. L. Shishkin, A. Finn, L. Smith, and M. Colket, "Image reconstruction for electrical capacitance tomography exploiting sparsity," in *Future of Instrumentation International Workshop (FIIW), 2012* (IEEE, 2012), pp. 1–4.

[19] W. Fang, "A nonlinear image reconstruction algorithm for electrical capacitance tomography," *Measurement Science and Technology* **15**, 2124 (2004).

[20] S. Jonsson, E.and Huang and T. Chan, "Total variation regularization in positron emission tomography," *CAM report* 98–48 (1998).

[21] A. Douiri, M. Schweiger, J. Riley, and S. R. Arridge, "Anisotropic diffusion regularization methods for diffuse optical tomography using edge prior information," *Measurement Science and Technology* **18**, 87 (2007).

[22] K. D. Paulsen and H. Jiang, "Enhanced frequency-domain optical image reconstruction in tissues through total-variation minimization," *Applied Optics* **35**, 3447–3458 (1996).

[23] Z. Tian, X. Jia, K. Yuan, T. Pan, and S. B. Jiang, "Low-dose CT reconstruction via edge-preserving total variation regularization," *Physics in Medicine and Biology* **56**, 5949 (2011).

[24] E. Y. Sidky and X. Pan, "Image reconstruction in circular cone-beam computed tomography by constrained, total-variation minimization," *Physics in Medicine and Biology* **53**, 4777 (2008).

[25] K. Hämäläinen, A. Kallonen, V. Kolehmainen, M. Lassas, K. Niinimäki, and S. Siltanen, "Sparse tomography," *SIAM Journal on Scientific Computing* **35**, B644–B665 (2013).

[26] E. Somersalo, J. P. Kaipio, V. Kolehmainen, and M. Vauhkonen, "Statistical inversion and Monte Carlo sampling methods in electrical impedance tomography," *Inverse Problems* **16**, 1487 (2000).

[27] A. Borsic and A. Adler, "A primal–dual interior-point framework for using the L_1 or L_2 norm on the data and regularization terms of inverse problems," *Inverse Problems* **28**, 095011 (2012).

[28] Y. Mamatjan, A. Borsic, D. Gürsoy, and A. Adler, "An experimental clinical evaluation of EIT imaging with L_1 data and image norms," *Physiological Measurement* **34**, 1027 (2013).

[29] L. Harhanen, N. Hyvönen, H. Majander, and S. Staboulis, "Edge-enhancing reconstruction algorithm for three-dimensional electrical impedance tomography," *arXiv preprint arXiv:1406.1279* (2014).

[30] G. González, J. M. J. Huttunen, V. Kolehmainen, A. Seppänen, and M. Vauhkonen, "Experimental evaluation of 3D electrical impedance tomography with total variation prior," *Inverse Problems in Science and Engineering* **24**, 1411–1431 (2016).

[31] P. Blomgren and T. Chan, "Color TV: total variation methods for restoration of vector-valued images," *IEEE transactions on image processing* **7**, 304–309 (1998).

[32] G. Sapiro and D. L. Ringach, "Anisotropic diffusion of multivalued images with applications to color filtering," *IEEE transactions on image processing* **5**, 1582–1586 (1996).

[33] R. Kimmel, R. Malladi, and N. Sochen, "Images as Embedded Maps and Minimal Surfaces: Movies, Color, Texture, and Volumetric Medical Images," *International Journal of Computer Vision* **39**, 111–129 (2000).

[34] M. Cheney, D. Isaacson, and J. C. Newell, "Electrical Impedance Tomography," *SIAM Review* **41**, 85–101 (1999).

[35] J. P. Kaipio, V. Kolehmainen, E. Somersalo, and M. Vauhkonen, "Statistical inversion and Monte Carlo sampling methods in electrical impedance tomography," *Inverse Problems* **16**, 1487 (2000).

[36] B. Brown, "Electrical impedance tomography (EIT): a review," *Journal of Medical Engineering & Technology* **27**, 97–108 (2003).

[37] D. S. Holder, "Electrical Impedance Tomography: Methods, History and Applications," *Medical Physics* **32**, 2731 (2005).

[38] J. Mueller and S. Siltanen, *Linear and Nonlinear Inverse Problems with Practical Applications* (SIAM, 2012).

[39] K. S. Cheng, D. Isaacson, J. Newell, and D. G. Gisser., "Electrode models for electric current computed tomography," *IEEE Transactions on Biomedical Engineering* **36**, 918–924 (1989).

[40] E. Somersalo, M. Cheney, and D. Isaacson, "Existence and uniqueness for electrode models for electric current computed tomography," *SIAM Journal on Applied Mathematics* **52**, 1023–1040 (1992).

[41] P. J. Vauhkonen, M. Vauhkonen, T. Savolainen, and J. P. Kaipio, "Three-dimensional electrical impedance tomography based on the complete electrode model," *IEEE Transactions on Biomedical Engineering* **46**, 1150–1160 (1999).

[42] A. Lipponen, A. Seppänen, and J. Kaipio, "Nonstationary inversion of convection-diffusion problems — recovery from unknown nonstationary velocity fields," *Inverse Problems Imaging* **4**, 463–83 (2010).

[43] A. Lipponen, A. Seppänen, and J. P. Kaipio, "Reduced-order estimation of non-stationary flows with electrical impedance tomography," *Inverse Problems* **26**, 074010 (2010).

[44] A. Lipponen, A. Seppänen, and J. P. Kaipio, "Nonstationary approximation error approach to imaging of three-dimensional pipe flow: experimental evaluation," *Measurement Science and Technology* **22**, 104013 (2011).

[45] S. J. Wright and J. Nocedal, *Numerical optimization* (Springer New York, 2006).

[46] S. Wright, "On the convergence of the Newton/log-barrier method," *Mathematical Programming* **90**, 71–100 (2001).

[47] A. V. Fiacco and G. McCormick, *Nonlinear programming: sequential unconstrained minimization techniques*, Vol. 4, (SIAM, 1990).

[48] J. L. Melsa and D. L. Cohn, *Decision and estimation theory* (McGraw-Hill, 1978).

[49] P. J. Vauhkonen, *Image Reconstruction in Three-Dimensional Electrical Impedance Tomography*, PhD thesis (University of Kuopio, Kuopio, Finland, 2004).

[50] A. P. Bagshaw, A. D. Liston, R. H. Bayford, A. Tizzard, A. P. Gibson, A. T. Tidswell, M. K. Sparkes, H. Dehghani, C. D. Binnie, and D. S. Holder, "Electrical impedance tomography of human brain function using reconstruction algorithms based on the finite element method," *NeuroImage* **20**, 752–764 (2003).

[51] B. H. Brown, D. C. Barber, and A. D. Seagar, "Applied potential tomography: possible clinical applications," *Clinical Physics and Physiological Measurement* **6**, 109 (1985).

[52] D. Barber and B. Brown, "Recent developments in applied potential tomography-APT," in *Information processing in medical imaging* (Springer, 1986), pp. 106–121.

[53] D. Barber and A. Seagar, "Fast reconstruction of resistance images," *Clinical Physics and Physiological Measurement* **8**, 47 (1987).

[54] M. Cheney, D. Isaacson, J. Newell, S. Simske, and J. Goble, "NOSER: An algorithm for solving the inverse conductivity problem," *International Journal of Imaging Systems and Technology* **2**, 66–75 (1990).

[55] R. Smallwood, A. Hampshire, B. Brown, R. Primhak, S. Marven, and P. Nopp, "A comparison of neonatal and adult lung impedances derived from EIT images," *Physiological Measurement* **20**, 401 (1999).

[56] R. Blue, D. Isaacson, and J. Newell, "Real-time three-dimensional electrical impedance imaging," *Physiological Measurement* **21**, 15 (2000).

[57] D. Holder and A. Khan, "Use of polyacrylamide gels in a saline-filled tank to determine the linearity of the Sheffield Mark 1 electrical impedance tomography (EIT) system in measuring impedance disturbances," *Physiological Measurement* **15**, A45 (1994).

[58] G. González, J. M. J. Huttunen, Kolehmainen, and M. Vauhkonen, "Joint reconstruction of conductivity and permittivity in EIT using structural similarity priors," *Inverse Problems in Science and Engineering* **XX**, XXX–XXX (2017).

[59] M. Lassas, E. Saksman, and S. Siltanen, "Discretization-invariant Bayesian inversion and Besov space priors," *Inverse Problems and Imaging* **3**, 87–122 (2009).

[60] M. Dashti, S. Harris, and A. Stuart, "Besov priors for Bayesian inverse problems," *Inverse Problems and Imaging* **6**, 183–200 (2012).

[61] J. P. Kaipio, V. Kolehmainen, E. Somersalo, and M. Vauhkonen, "Statistical inversion and Monte Carlo sampling methods in electrical impedance tomography," *Inverse Problems* **16**, 1487 (2000).

[62] S. Hamilton, A. Hauptmann, and S. Siltanen, "A data-driven edge-preserving D-bar method for electrical impedance tomography," *Inverse Problems and Imaging* **8**, 1053–1072 (2014).

[63] B. Jin, T. Khan, and P. Maass, "A reconstruction algorithm for electrical impedance tomography based on sparsity regularization," *International Journal for Numerical Methods in Engineering* **89**, 337–353 (2012).

[64] V. Mazja, *Sobolev Spaces* (Springer-Verlag, Berlin, 1985).

[65] H. Attouch, G. Buttazzo, and G. Michaille, *Variational analysis in Sobolev and BV spaces: applications to PDEs and optimization* (SIAM, 2014).

[66] L. Gallardo and M. Meju, "Characterization of heterogeneous near-surface materials by joint 2D inversion of DC resistivity and seismic data," *Geophysical Research Letters* **30** (2003).

[67] E. Haber and M. Gazit, "Model fusion and joint inversion," *Surveys in Geophysics* **34**, 675–695 (2013).

[68] P. Hansen, "Analysis of discrete ill-posed problems by means of the L-curve," *SIAM review* **34**, 561–580 (1992).

[69] P. Blomgren and T. Chan, "Modular solvers for image restoration problems using the discrepancy principle," *Numerical linear algebra with applications* **9**, 347–358 (2002).

[70] L. Calatroni, C. Chung, J. Reyes, C. Schönlieb, and T. Valkonen, "Bilevel approaches for learning of variational imaging models," *arXiv preprint arXiv:1505.02120* (2015).

[71] K. Kunisch and T. Pock, "A bilevel optimization approach for parameter learning in variational models," *SIAM Journal on Imaging Sciences* **6**, 938–983 (2013).

[72] J. Kourunen, T. Savolainen, A. Lehikoinen, M. Vauhkonen, and L. M. Heikkinen, "Suitability of a PXI platform for an electrical impedance tomography system," *Measurement Science and Technology* **20**, 015503 (2009).

[73] Z. Wang, A. Bovik, H. Sheikh, and E. Simoncelli, "Image quality assessment: from error visibility to structural similarity," *Image Processing, IEEE Transactions on* **13**, 600–612 (2004).

[74] S. Hamilton and J. Mueller, "Direct EIT reconstructions of complex admittivities on a chest-shaped domain in 2-D," *Medical Imaging, IEEE Transactions on* **32**, 757–769 (2013).

GERARDO GONZÁLEZ

In electrical impedance tomography (EIT), the conductivity and permittivity distributions of a target are reconstructed based on voltage measurements, known current injections, and knowledge of the target geometry. Due to the ill-posedness of this reconstruction problem, the determination of a meaningful solution depends heavily on the prior information related to the target. In this thesis, prior models based on the total variation (TV) functional are used to improve the quality of the conductivity and permittivity reconstructions. The findings presented in this thesis demonstrate the feasibility of the proposed prior models for reconstructing the conductivity and permittivity in the presence of noise.

UNIVERSITY OF
EASTERN FINLAND

uef.fi

PUBLICATIONS OF
THE UNIVERSITY OF EASTERN FINLAND
Dissertations in Forestry and Natural Sciences

ISBN 978-952-61-2671-5
ISSN 1798-5668